Topography curvature effects in thin-layer models for gravity-driven flows without bed erosion

Marc Peruzzetto, Anne Mangeney, François Bouchut, Gilles Grandjean, Clara Lévy, Yannick Thiery, Antoine Lucas

▶ **To cite this version:**

Marc Peruzzetto, Anne Mangeney, François Bouchut, Gilles Grandjean, Clara Lévy, et al.. Topography curvature effects in thin-layer models for gravity-driven flows without bed erosion. Journal of Geophysical Research: Earth Surface, 2021, 126 (4), pp.e2020JF005657. ⟨10.1029/2020JF005657⟩. ⟨hal-03039631⟩

HAL Id: hal-03039631

https://hal.science/hal-03039631v1

Submitted on 4 Dec 2020

HAL is a multi-disciplinary open access archive for the deposit and dissemination of scientific research documents, whether they are published or not. The documents may come from teaching and research institutions in France or abroad, or from public or private research centers.

L'archive ouverte pluridisciplinaire **HAL**, est destinée au dépôt et à la diffusion de documents scientifiques de niveau recherche, publiés ou non, émanant des établissements d'enseignement et de recherche français ou étrangers, des laboratoires publics ou privés.

HAL Authorization

Topography curvature effects in thin-layer models for gravity-driven flows without bed erosion

Marc Peruzzetto[1,2], Anne Mangeney[1], François Bouchut[3], Gilles Grandjean[2], Clara Levy[2], Yannick Thiery[2]and Antoine Lucas[1]

[1]Université de Paris, Institut de physique du globe de Paris, CNRS, F-75005 Paris, France.
[2]BRGM, Orléans, France.
[3]Laboratoire d'Analyse et de Mathématiques Appliquées (UMR 8050), CNRS, Univ. Gustave Eiffel, UPEC, Marne-la-Vallée F-77454, France

Key Points:

- Interpretation of topography curvature terms in thin-layer models.
- Comparison of methods to include curvature effects in thin-layer models.
- Quantification of curvature effects in thin-layer model simulations with synthetic and real topographies.

Corresponding author: Marc Peruzzetto, peruzzetto@ipgp.fr

Abstract

Depth-averaged thin-layer models are commonly used to model rapid gravity-driven flows such as debris flows or debris avalanches. However, the formal derivation of thin-layer equations for general topographies is not straightforward. The curvature of the topography results in a force that keeps the velocity tangent to the topography. Another curvature term appears in the bottom friction force when frictional rheologies are used. In this work, we present the main lines of the mathematical derivation for these curvature terms that are proportional to the square velocity. Then, with the SHALTOP numerical model, we quantify their influence on flow dynamics and deposits over synthetic and real topographies. This is done by comparing simulations in which curvature terms are exact, disregarded or approximated. With the Coulomb rheology, for slopes $\theta = 10°$ and for friction coefficients below $\mu = \tan(5°)$, neglecting the curvature force increases travel times by up to 10% and 30%, for synthetic and real topographies respectively. When the curvature in the friction force is neglected, the travel distance may be increased by several hundred meters on real topographies, whatever the topography slopes and friction coefficients. We observe similar effects on a synthetic channel with slope $\theta = 25°$ and $\mu = \tan(15°)$, with a 50% increase of the kinetic energy. Finally, approximations of curvature in the friction force can break the non-invariance of the equations and decelerate the flow. With the Voellmy rheology, these discrepancies are less significant. Curvature effects can thus have significant impact for model calibration and for overflows prediction, both being critical for hazard assessment.

1 Introduction

The propagation of rapid gravity-driven flows [*Iverson and Denlinger*, 2001] occurring in mountainous or volcanic areas is a complex and hazardous phenomenon. A wide variety of events are associated with these flows, such as rock avalanches, debris avalanches and debris, mud or hyper-concentrated flows [*Hungr et al.*, 2014]. The understanding and estimation of their propagation processes is important for sediment fluxes quantification, for the study of landscapes dynamics. Besides, gravity-driven flows can have a significant economic impact and endanger local populations [*Hungr et al.*, 2005; *Petley*, 2012; *Froude and Petley*, 2018]. In order to mitigate these risks, it is of prior importance to estimate the runout, dynamic impact and travel time of potential gravitational flows.

This can be done empirically, but physically-based modeling is needed to investigate more precisely the dynamics of the flow, in particular due to the first-order role of local topography. Over the past decades, thin-layer models (also called shallow-water models) have been increasingly used by practictioners. Their main assumption is that the flow extent is much larger than its thickness, so that the kinematic unknowns are reduced to two variables: the flow thickness and its depth-averaged velocity. The dimension of the problem is thus lower, allowing for relatively fast numerical computations. The first and simplest form of thin-layer equations was given by *Barré de Saint-Venant* [1871] for almost flat topographies. The 1D formulation (i.e. for topographies given by a 1D graph $Z = Z(X)$) for any bed inclination and small curvatures was derived by *Savage and Hutter* [1991]. This model has since been extended to real 2D topographies (i.e. given by a 2D graph $Z = Z(X, Y)$). Some of the software products based on thin-layer equations are currently used for hazard assessment to derive, for instance, maps of maximum flow height and velocity. Examples include RAMMS [*Christen et al.*, 2010, 2012], 3d-DMM [*GEO*, 2011; *Law et al.*, 2017], DAN3D [*McDougall and Hungr*, 2004; *Moase et al.*, 2018] and FLO-2D [*O'Brien et al.*, 1993]. A non exhaustive overview of some existing models used for field scale modeling is given in Table 1. *Yavari-Ramshe and Ataie-Ashtiani* [2016] and *Delannay et al.* [2017] give a more comprehensive review of thin-layer models. Current research focuses include modeling of multi-layer flows [*Fernández-Nieto et al.*, 2018; *Garres-Díaz et al.*, 2020], bed erosion along the flow path [*Hungr*, 1995; *Bouchut et al.*, 2008; *Iverson*, 2012; *Pirulli and Pastor*, 2012] and the description of two-phase flows [e.g.

Pudasaini, 2012; *Rosatti and Begnudelli*, 2013; *Iverson and George*, 2014; *Bouchut et al.*, 2015, 2016; *Pastor et al.*, 2018a].

In addition to the complexity of choosing realistic constitutive equations to model the flow physical properties, there is also a purely methodological difficulty in deriving the thin-layer equations for a complex topography, with acceleration forces arising from the curvature of the topography. Their influence in 1D thin-layer models was investigated by *Hutter and Koch* [1991], *Greve and Hutter* [1993] and *Bouchut et al.* [2003]. *Koch et al.* [1994] investigated curvature effects for unconfined flows on simple 2D topographies. Their work was completed by *Gray et al.* [1999] and *Wieland et al.* [1999] for channelized flows in straight channels. Later on *Pudasaini and Hutter* [2003] and *Pudasaini et al.* [2003] considered flows in curved and twisted channels. The generalization of curvature forces to general topographies was done by *Bouchut and Westdickenberg* [2004], *Luca et al.* [2009a] and *Rauter and Tukovic* [2018]. To our knowledge, only one study focused on quantifying curvature effects in simulations on general topographies: *Fischer et al.* [2012] showed curtaure terms have a substantial effect for model calibration. However, it focuses on curvature terms in the bottom friction and does not consider other curvature terms that are independent from the chosen rheology.

In this work, we aim at quantifying more generally and precisely the influence of curvature terms in depth-averaged thin-layers simulations. This is important for practitioners using thin-layers models: we will identify situations (in terms of topographic settings and rheological parametrization) where curvature effects may significantly impact their simulation results, and thus are worth taking into account for hazard assessment. We focus on the modeling of single-phase incompressible flows, with an Eulerian description. We also disregard bed erosion and internal friction. The resulting equations may be oversimplified in comparison to the physical processes at stake in real geophysical flows. However, such equations are now widely used to simulate debris flows, debris avalanches and rock avalanches [*Hungr et al.*, 2007; *Pastor et al.*, 2018b]. Thus, we deem important to assess quantitavely the importance of curvature terms for field applications. However, we acknowledge that it goes along with major uncertainties on the rheology and rheological parameters needed to reproduce correctly real gravity flows.

In the following section, we present the depth-averaged thin-layer equations for flows on complex topographies . We detail the derivation of two curvature terms: one that does not depend on the rheology and the other appearing in the bottom friction when a frictional rheology is used. We also introduce the SHALTOP numerical model [*Mangeney et al.*, 2007] and its modified version without curvature forces, that will be used to carry out simulations. The curvature terms will be formally analyzed and compared to previous studies in Section 3. Then, in Section 4, we illustrate for synthetic topographies the importance of taking into account curvature forces. Finally, in Section 5, we consider two real Digital Elevation Models, with a non-viscous debris flow in the Prêcheur river (Martinique, French Caribbean) and a potential massive debris avalanche from the Soufrière de Guadeloupe volcano (Guadeloupe, French Caribbean).

2 Modeling approach using thin-layer equations

Thin-layer equations model the propagation of a thin layer of fluid following the topography . As opposed to full 3D models, thin-layer models no longer simulate the movement of each solid or fluid element. Instead, they integrate their dynamics over a column of fluid in the direction normal to the topography and consider the mean flow velocity over this column. Although the resulting equations are relatively simple, their rigorous derivation is not straight-forward. As a matter of fact, the momentum and mass equations must first be written in a reference frame that allows a convenient integration. Its mere definition is difficult, not to mention the expression of the constitutive equations in the resulting coordinate system. In Supplementary Note 1, we describe into details how cur-

Table 1. Non exhaustive list of 2D thin-layer models used at the field scale.

Model name	**Numerical scheme**	**Bed erosion**	**Two-phase flows**	**References**
MassMov2D	Finite Differences	-	-	[*Beguería et al.*, 2009]
Flo-2D		-	-	[*O'Brien et al.*, 1993]
Volcflow		x	-	[*Kelfoun and Druitt*, 2005]
SHALTOP	Finite Volumes	-	-	[*Bouchut and Westdickenberg*, 2004; *Mangeney et al.*, 2007]
RAMMS		x	-	[*Christen et al.*, 2010]
RASH3D		x	-	[*Pirulli et al.*, 2007; *Pirulli and Pastor*, 2012]
r.avaflow		x	x	[*Pudasaini*, 2012; *Mergili et al.*, 2017]
GeoClaw		-	-	[*Berger et al.*, 2011; *LeVeque et al.*, 2011]
D-Claw		-	x	[*Iverson and George*, 2014; *George and Iverson*, 2014]
Titan2D		-	x	[*Patra et al.*, 2005; *Pitman and Le*, 2005]
TRENT-2D		-	x	[*Armanini et al.*, 2009; *Rosatti and Begnudelli*, 2013]
DAN3D	SPH (Smoothed Particle Hydrodynamics)	x	-	[*McDougall and Hungr*, 2004]
GeoFlow_SPH		x	x	[*Pastor et al.*, 2009a, 2018a]
3d-DMM		x	-	[*Kwan and Sun*, 2007; *Law et al.*, 2017]

vature terms appear in the thin-layer equations derivation in *Bouchut and Westdickenberg* [2004]. In the following, we will only present the chosen parametrization and the final equations.

2.1 Mass and momentum equations and boundary conditions

Most thin-layer models are based on the incompressible mass and momentum equations

$$\partial_t \vec{U} + (\vec{U} \cdot \nabla_{\vec{X}})\vec{U} = -\vec{g} + \nabla_{\vec{X}} \cdot \sigma, \tag{1}$$

$$\nabla_{\vec{X}} \cdot \vec{U} = 0, \tag{2}$$

where $-\vec{g}$ is gravity and σ the Cauchy stress tensor normalized by the flow density. $\vec{X} = (X, Y, Z)$ is the cartesian coordinate system associated with the orthonormal base $(\vec{e}_X, \vec{e}_Y, \vec{e}_Z)$. In the following we will write $\mathbf{X} = (X, Y) \in \mathbb{R}^2$ for the horizontal coordinates. In the following, 3D vectors will be identified by an arrow and 2D vectors will be in bold. For instance, $\vec{U}(\vec{X}) = (U_X, U_Y, U_Z) = (\mathbf{U}, U_Z)$ gives the components of the 3D velocity field in the cartesian reference frame. $\nabla_{\vec{X}}$ is the gradient operator.

The base of the flow matches the topography and is given by a 2D surface $Z = b(\mathbf{X})$, with upward unit normal vector $\vec{n}$ (Figure 1a for 1D topographies, Figure 1b for 2D topographies),

$$\vec{n} = c\Big(-\frac{\partial b}{\partial X}, -\frac{\partial b}{\partial Y}, 1\Big) = \Big(-\mathbf{s}, c\Big), \tag{3}$$

with

$$c = \cos(\theta) = \Big(1 + \|\nabla_{\mathbf{X}} b\|^2\Big)^{-\frac{1}{2}}, \tag{4}$$

$$\mathbf{s} = c\nabla_{\mathbf{X}} b, \tag{5}$$

where θ is the topography steepest slope angle. Along with boundary conditions detailed in Supplementary Note 1, a constitutive equation for the stress tensor σ is needed to close the problem. The latter can be divided into pressure and deviatoric parts, namely

$$\sigma = \sigma' - pI_3, \tag{6}$$

with σ' the deviatoric stress tensor, p the pressure field (devided by the flow density) and I_3 the identity matrix. For scale analysis and to allow for a rigorous mathematical derivation, *Bouchut and Westdickenberg* [2004] chose a Newtonian approach with a linear stress constitutive equation

$$\sigma' = \nu\left(\nabla_{\vec{X}}\vec{U} + (\nabla_{\vec{X}}\vec{U})^t\right), \tag{7}$$

with ν the kinematic viscosity, that is assumed to be small (see Supplementary Note 1). They furthermore imposed a friction boundary condition at the bed

$$\sigma\vec{n} - (\vec{n} \cdot \sigma\vec{n})\,\vec{n} = \mu\frac{\vec{U}}{\|\vec{U}\|}(-\vec{n} \cdot \sigma\vec{n})_+, \tag{8}$$

where $\mu = \tan(\delta)$ is the friction coefficient and δ is the friction angle. The key point here is the transformation of the equations in a convenient reference frame, in which they can be integrated.

2.2 Coordinate system and reference frame

The simplest way to derive the thin-layer equations is to use cartesian coordinates and integrate the Navier-Stoke equations along the vertical direction [*Barré de Saint-Venant*, 1871; *Pitman et al.*, 2003; *Berger et al.*, 2011]. This is done in particular to model the propagation of tsunamis because the wavelength of waves is small in comparison to the

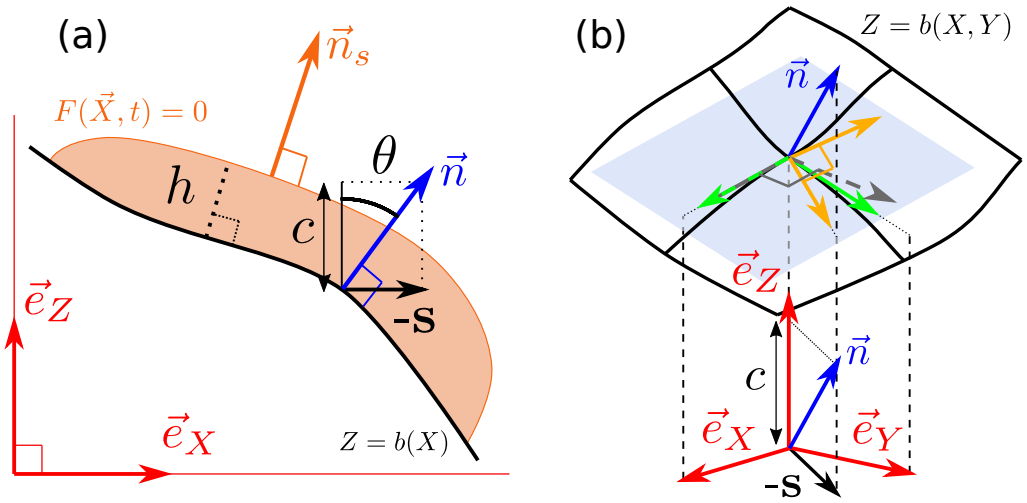

Figure 1. (a) Topography and flow description, for a 1D topography $Z = b(X)$. The orange area is the flow region, with thickness h in the direction normal to the topography. (b) 2D topography $Z = b(X,Y)$ description, with reference frames commonly used in the literature to derive thin-layer equations. Red arrows: Cartesian reference frame. Blue arrows: topography normal unit vector. $-\mathbf{s}$: main slope horizontal direction. All other arrows are in the topography tangent plane (blue plane). Green arrows: *Christen et al.* [2010]. Dashed gray arrows: *Mangeney-Castelnau et al.* [2003]. Orange arrows: *Iverson and George* [2014].

water vertical depth and the main driving forces are horizontal pressure gradients [e.g. *Berger et al.*, 2011; *LeVeque et al.*, 2011]. On the contrary, the shallowness of landslides propagating on potentially steep slopes must be regarded in the direction normal to the topography. Moreover, the flow velocity is (at least for a first approximation) tangent to the topography. Thus the velocity in the normal direction is small. In order to translate this property it is appropriate to write these equations in a reference frame linked to the topography with one vector in the direction normal to the topography. In Figure 1b, we give some reference frames used in previous studies. A proper definition is of prior importance, as the reference frame varies spatially. Spatial differential operators in the flow equations, with respect to this reference frame, will thus describe the spatial variations of the fluid thickness and velocity as well as the variations of the reference frame itself.

In order to characterize these variations, a functional relation must be found to relate the new coordinates to the cartesian coordinates, from which the spatial derivative operators in the new reference frame can be deduced. It is therefore somehow more natural and mathematically simple to first define the new coordinate system and to derive the associated reference frame, instead of the contrary. With this method, the reference frame may not be orthonormal but this does not entail any loss of generality or accuracy compared to models using an orthonormal reference frame.

The most straightforward way to localize a point M above the topography is to consider its projection M' on the topography, along the direction normal to the topography (Figure 2a). The point M, which has coordinates $\vec{X} = (X, Y, Z)$ in the cartesian reference frame, can then be localized with a new set of coordinates (x_1, x_2, x_3): $(x_1, x_2) = \mathbf{x}$ are the horizontal coordinates of M' in the cartesian reference frame and $x_3 = MM'$ is the distance to the topography (Figure 2a). Provided we remain in a sufficiently small neighborhood above the topography, this new coordinate system is non-ambiguous: one (and only one) triplet (x_1, x_2, x_3) can be associated with any point in this neighborhood and vice-versa. More formally, the link between the cartesian coordinates $\vec{X} = (\mathbf{X}, Z)$ and the new

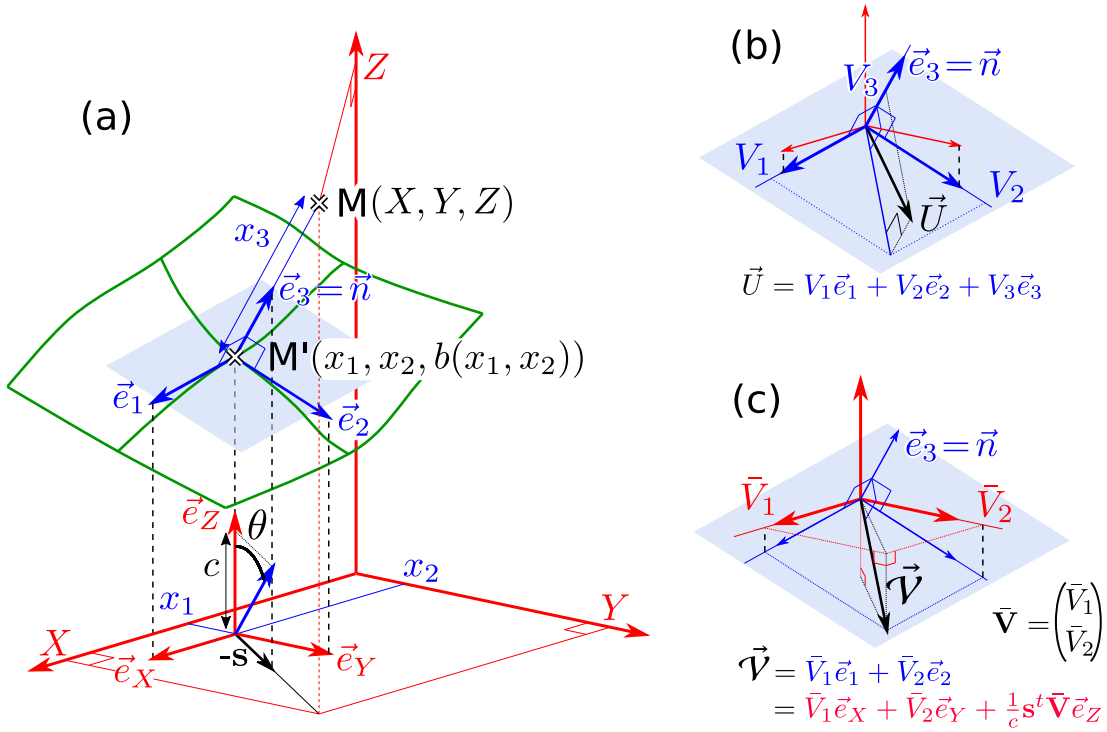

Figure 2. Notations and reference frames for the thin-layer equation derivations. (a) Coordinates of a material point M in the cartesian reference frame $(\vec{e}_X, \vec{e}_Y, \vec{e}_Z)$ (red arrows) are given by (X, Y, Z) and by (x_1, x_2, x_3) in the topography reference frame $(\vec{e}_1, \vec{e}_2, \vec{e}_3)$ (blues arrows). M' is the projection of M on the topography: it has cartesian coordinates $(x_1, x_2, b(x_1, x_2))$. $\vec{e}_3$ is the unit normal vector to the topography and $\vec{e}_1$, $\vec{e}_2$ are the projections parallel to $\vec{e}_Z$ of $\vec{e}_X$ and $\vec{e}_Y$ on the plane tangent to the topography (blue feature). (b) Parametrization of the physical velocity $\vec{U}$ of a material point in the topography reference frame. (c) Parametrization of the physical average velocity $\vec{\mathcal{V}}$ of the flow. $\vec{\mathcal{V}}$ is tangent to the topography and is parametrized in the cartesian reference frame (red) and in the topography reference frame (blue).

coordinates $\vec{x} = (x_1, x_2, x_3) = (\mathbf{x}, x_3)$ of a same physical point is given by

$$(\mathbf{X}, Z) = \vec{X}(\mathbf{x}, x_3) = M' + x_3\vec{n} = \begin{pmatrix} \mathbf{x} \\ b(\mathbf{x}) \end{pmatrix} + x_3\vec{n}(\mathbf{x}). \tag{9}$$

As previously, $\vec{n} = \vec{n}(\mathbf{x})$ is the unit upward vector normal to the topography. The same coordinate system was used by *Bouchut et al.* [2003] for 1D topographies and *Bouchut and Westdickenberg* [2004] and *Luca et al.* [2009a] for 2D topographies. A more general formulation with a curvilinear coordinate system $\mathbf{x} = \mathbf{x}(\boldsymbol{\xi})$ is presented in *Bouchut and Westdickenberg* [2004]. For instance, for 1D topographies, we can choose to locate M' by its curvilinear coordinates along the topography, instead of its cartesian X-coordinate [*Savage and Hutter*, 1991]. For simplicity, we shall keep the Cartesian coordinate system to locate M'. However, this does not limit in any way the type of topographies that can be described in the model.

The reference frame $(\vec{e}_1, \vec{e}_2, \vec{e}_3)$ associated with the new coordinates $\vec{x} = (x_1, x_2, x_3)$ follows coordinate lines, so we obtain, with the Einstein notation

$$d\vec{X} = \vec{e}_i dx_i = \vec{e}_1 dx_1 + \vec{e}_2 dx_2 + \vec{e}_3 dx_3. \tag{10}$$

We therefore have, for instance, $\vec{e}_1 = \partial_{x_1}\vec{X}$. In this base, the velocity field has coordinates $\vec{V} = (V_1, V_2, V_3) = (\mathbf{V}, V_3)$, such that (Figure 2b)

$$\vec{U} = U_X\vec{e}_X + U_Y\vec{e}_Y + U_Z\vec{e}_Z = V_1\vec{e}_1 + V_2\vec{e}_2 + V_3\vec{e}_3. \tag{11}$$

We can show (see Supplementary Note 1) that $\vec{e}_3 = \vec{n}$ and thus that V_3 is the topography normal component of the velocity (Figure 2b).

Note that in the previous equation, $\vec{U}$ must be seen as the physical 3D velocity of the fluid, in the sense that $\|\vec{U}\| = \left(U_X^2 + U_Y^2 + U_Z^2\right)^{\frac{1}{2}}$ is the real velocity. In comparison, $\vec{V}$ is only a parametrization of the velocity field. In particular, as the topography reference frame is in general not orthonormal, we have

$$\|\vec{V}\| = \left(V_1^2 + V_2^2 + V_3^2\right)^{\frac{1}{2}} \neq \|\vec{U}\|. \tag{12}$$

It is not straightforward to replace $\vec{U}$ by $\vec{V}$ in the Navier-Stokes equations . This derivation can be found in [*Bouchut and Westdickenberg*, 2004], or in [*Luca et al.*, 2009a] with a different formalism. However, the resulting equations can be significantly simplified with the thin-layer approximations. In the following, we simply give the final thin-layer equations and analyze the resulting curvature terms. More details on the formal derivation and hypotheses are given in Supplementary Note 1.

2.3 Thin-layer equations

In the thin-layer approximation, we describe the dynamics of a fluid layer with thickness $h(\mathbf{x})$. We assume this thickness to be small in comparison to the flow extent. Its physical depth-averaged velocity $\vec{\mathcal{V}}$ is tangent to the topography and thus can be written in the topography frame

$$\vec{\mathcal{V}} = \bar{V}_1\vec{e}_1 + \bar{V}_2\vec{e}_2 \tag{13}$$

and has coordinates $(\boldsymbol{\mathcal{V}}, \mathcal{V}_3)$ in the cartesian coordinate system. We can show (see Supplementary Note 1) that it is written in the cartesian reference frame:

$$\vec{\mathcal{V}} = \bar{V}_1\vec{e}_X + \bar{V}_2\vec{e}_Y + \frac{1}{c}\mathbf{s}^t\bar{\mathbf{V}}\vec{e}_Z \tag{14}$$

We show that $\bar{V}_1\vec{e}_1$ and $\bar{V}_2\vec{e}_2$ are respectively the projections of $\bar{V}_1\vec{e}_X$ and $\bar{V}_2\vec{e}_Y$, on the topography-tangent plane, parallel to $\vec{e}_Z$ (Figure 2c).

The resulting equation for $\bar{\mathbf{V}} = (\bar{V}_1, \bar{V}_2)$ is given by

$$\partial_t\bar{\mathbf{V}} + (\bar{\mathbf{V}}\cdot\nabla_{\mathbf{x}})\bar{\mathbf{V}} + (I_2 - \mathbf{s}\mathbf{s}^t)\nabla_{\mathbf{x}}\left(g(hc+b)\right) = -c\left(\bar{\mathbf{V}}^t(\partial^2_{\mathbf{xx}}b)\bar{\mathbf{V}}\right)\mathbf{s} - \frac{\mu g c\bar{\mathbf{V}}}{\sqrt{\|\bar{\mathbf{V}}\|^2 + \left(\frac{1}{c}\mathbf{s}^t\bar{\mathbf{V}}\right)^2}}\left(1 + \frac{\bar{\mathbf{V}}^t(\partial^2_{\mathbf{xx}}b)\bar{\mathbf{V}}}{g}\right)_+. \tag{15}$$

Two curvature terms, involving $\partial^2_{\mathbf{xx}}b$, appear in (15). One does not depend on the rheology (red term in (15)) and the other is included in the friction force (blue term in (15)). These terms arise from the expression of the pressure at the bottom of the flow (see Supplementary Note 1). They will be interpreted in Section 3. Note that (15) is equivalent to equation (9.32) in *Luca et al.* [2009a]. The viscosity ν does not appear in (15), because we chose it to be negligible, which allows for a rigorous mathematical derivation. To our knowledge, there exist no formal derivation of thin-layer equations with non negligible viscosity, an no assumption on the velocity profile, on general topographies.

The mass equation does not entail any curvature term. With the same formalism as in our development, *Bouchut and Westdickenberg* [2004] show that it reads :

$$\partial_t\left(\frac{h}{c}\right) + \nabla_{\mathbf{x}}\cdot\left(\frac{h}{c}\bar{\mathbf{V}}\right) = 0. \tag{16}$$

2.4 The SHALTOP numerical model

In order to investigate the influence of curvature forces in numerical simulations, we use the SHALTOP numerical model [*Mangeney et al.*, 2007]. It has been used to reproduce both experimental dry granular flows [*Mangeney et al.*, 2007] and real landslides [*Lucas and Mangeney*, 2007; *Favreau et al.*, 2010; *Lucas et al.*, 2011, 2014; *Moretti et al.*, 2015, 2020; *Brunet et al.*, 2017; *Peruzzetto et al.*, 2019]. We choose not to compare SHALTOP to another code that would not describe precisely the topography effects. We would not be able to tell whether discrepancies in results originate from curvature effects or, for instance, from the different numerical scheme. A proper benchmarking exercise would be needed, but is beyond the scope of this work. Instead we shall use the same code, but modify it in order to reflect several approximations or remove the curvature .

In SHALTOP, the flow equations are written in terms of the variable $\mathbf{u} = \bar{\mathbf{V}}/c$. This parametrization will be discuss later on. The corresponding momentum equation is:

$$\begin{aligned}\partial_t \mathbf{u} + c(\mathbf{u}\cdot\nabla_{\mathbf{x}})\mathbf{u} + \frac{1}{c}(Id - \mathbf{s}\mathbf{s}^t)\nabla_{\mathbf{x}}\left(g(hc+b)\right) \\ = -\frac{1}{c}\left(\mathbf{u}^t\mathcal{H}\mathbf{u}\right)\mathbf{s} + \frac{1}{c}\left(\mathbf{s}^t\mathcal{H}\mathbf{u}\right)\mathbf{u} - \frac{\mu g c\mathbf{u}}{\sqrt{c^2\|\mathbf{u}\|^2 + (\mathbf{s}^t\mathbf{u})^2}}\left(1 + \frac{c^2\mathbf{u}^t(\partial^2_{\mathbf{xx}}b)\mathbf{u}}{g}\right).\end{aligned} \tag{17}$$

with curvature terms colored as in (15). SHALTOP solves the conservative form of (17) with a finite-volume numerical scheme (see *Mangeney et al.* [2007]

We will show in Section 3.1 that the curvature force (first two terms on the right-hand side of (17)) ensures the velocity remains tangent to the topography at all time. Thus, to model this effect, a tangent transport is applied [e.g. *Knebelman*, 1951]. Considering the physical velocity $\vec{\mathcal{V}} = (c\mathbf{u}, \mathbf{s}^t\mathbf{u})$ in one cell with topography normal vectors $\vec{n}$, the transported velocity $\vec{\mathcal{V}}'$ in a neighboring cell with normal vector $\vec{n}'$ is computed with:

$$\vec{\mathcal{V}}' = \vec{\mathcal{V}} - \frac{\vec{\mathcal{V}}\cdot\vec{n}'}{1+\vec{n}\cdot\vec{n}'}\left(\vec{n}+\vec{n}'\right) \tag{18}$$

Since the curvature force involves the slope variations, for real data with small scale variations it is often necessary to slightly smooth the topography to avoid numerical instabilities. Indeed, when the topography radius of curvature is smaller than the flow thickness, lines normal to the topographies can cross within the flow. In turn the coordinate system defined in (9) is ambiguous: several coordinates (x_1, x_2, x_3) can be associated to a single physical point.

In SHALTOP, the friction coefficient μ can be a function of the flow thickness and velocity. We can thus change the expression of the bottom stress T as in other classical rheologies. For instance, in the semi-empirical Voellmy rheology [*Voellmy*, 1955; *Salm*, 1993], the bottom stress reads:

$$T = \rho h\mu(gc + \gamma\|\vec{\mathcal{V}}\|^2) + \rho g\frac{\|\vec{\mathcal{V}}\|^2}{\xi}, \tag{19}$$

with ρ the material density, γ the curvature along flow path (see next section for its computation) and ξ the turbulence coefficient. In numerical experiments (Sections 4 and (5)), we will consider both the Coulomb and the Voellmy rheology that are classically used for field application due to the small number of parameters involved while being able to reproduce first order observations [e.g. *Hungr et al.*, 2007; *Lucas et al.*, 2014; *McDougall*, 2017].

3 Formal analysis of curvature terms

3.1 Interpretation of curvature terms

The curvature terms appearing in the derived thin-layer equations can be interpreted as acceleration forces in the non-Galilean reference frame linked to the topography. This appears more clearly when we write the depth-averaged equations for the 3D velocity $\vec{\mathcal{V}}$, in the cartesian reference frame :

$$\partial_t \vec{\mathcal{V}} + (\boldsymbol{\mathcal{V}} \cdot \nabla_{\mathbf{X}} \vec{\mathcal{V}}) = \vec{F}_g + \vec{F}_{\mathcal{H}} + \vec{F}_\mu, \tag{20}$$

with

$$\vec{F}_g = -\begin{pmatrix} Id - \mathbf{s}\mathbf{s}^t \\ c\mathbf{s}^t \end{pmatrix} \nabla_{\mathbf{X}}(g(hc+b)), \tag{21}$$

$$\vec{F}_{\mathcal{H}} = c(\boldsymbol{\mathcal{V}}^t \partial^2_{\mathbf{XX}} b \boldsymbol{\mathcal{V}})\vec{n} = \frac{1}{c^2}(\boldsymbol{\mathcal{V}}^t \mathcal{H} \boldsymbol{\mathcal{V}})\vec{n}, \tag{22}$$

$$\vec{F}_\mu = -\frac{\mu g c \vec{\mathcal{V}}}{\|\vec{\mathcal{V}}\|}\left(1 + \frac{\boldsymbol{\mathcal{V}}^t(\partial^2_{\mathbf{XX}} b)\boldsymbol{\mathcal{V}}}{g}\right)_+, \tag{23}$$

where $\mathcal{H} = c^3 \partial^2_{\mathbf{XX}} b$ is the curvature tensor. $\vec{F}_g$ represents the gravity and lateral pressure forces, $\vec{F}_\mu$ is the friction force and $\vec{F}_{\mathcal{H}}$ is the curvature force.

For a material point advected by the velocity field $\vec{\mathcal{V}}$, we can compute

$$\frac{d}{dt}(\vec{\mathcal{V}} \cdot \vec{n}) = \left(\partial_t \vec{\mathcal{V}} + (\boldsymbol{\mathcal{V}} \cdot \nabla_{\mathbf{X}})\vec{\mathcal{V}}\right) \cdot \vec{n} + \vec{\mathcal{V}} \cdot \left((\boldsymbol{\mathcal{V}} \cdot \nabla_{\mathbf{X}})\vec{n}\right) \tag{24}$$

$$= \left(\partial_t \vec{\mathcal{V}} + (\boldsymbol{\mathcal{V}} \cdot \nabla_{\mathbf{X}})\vec{\mathcal{V}}\right) \cdot \vec{n} - c\boldsymbol{\mathcal{V}}^t \partial^2_{\mathbf{XX}} b \boldsymbol{\mathcal{V}}. \tag{25}$$

In the right-hand side of (24), we can use (20). As $\vec{F}_g \cdot \vec{n} = \vec{F}_\mu \cdot \vec{n} = 0$ and $\vec{F}_{\mathcal{H}} \cdot \vec{n} = c\boldsymbol{\mathcal{V}}^t \partial^2_{\mathbf{XX}} b \boldsymbol{\mathcal{V}}$, (24) becomes

$$\frac{d}{dt}(\vec{\mathcal{V}} \cdot \vec{n}) = 0. \tag{26}$$

In other words, the curvature force $\vec{F}_{\mathcal{H}}$ ensures that the flow velocity remains parallel to the topography, i.e. $\vec{\mathcal{V}} \cdot \vec{n} = 0$. This force is normal to the topography and thus to the velocity and does no work: in the absence of gravity and friction, the material point would be advected on the topography at constant kinetic energy. Note that this acceleration force is still present, though the equations are written in the fixed cartesian coordinate system: that's because they arise in the intermediate step where the momentum equations are integrated in the direction normal to the topography. The Lagrangian form of equation (20) provides a direct expression of the curvature along a flow path. As a matter of fact, if $M(t)$ is the position of a material point, we have

$$\dot{M}(t) = \vec{\mathcal{V}}, \tag{27}$$

$$\ddot{M}(t) = \partial_t \vec{\mathcal{V}} + \boldsymbol{\mathcal{V}} \cdot \nabla_{\mathbf{X}} \vec{\mathcal{V}}. \tag{28}$$

From classical analytical geometry results and using (20), the curvature of the topography along a flow path, γ, is thus given by

$$\gamma = \pm \frac{\left\|\dot{M} \wedge \ddot{M}\right\|}{\left\|\dot{M}\right\|^3} = c\frac{\boldsymbol{\mathcal{V}}^t \partial^2_{\mathbf{XX}} b \boldsymbol{\mathcal{V}}}{\|\vec{\mathcal{V}}\|^2}. \tag{29}$$

In the previous equation, we used (28) and (20), and the fact that $\vec{F}_{\mathcal{H}}$ is the only force which is not colinear to the velovity $\dot{M} = \vec{\mathcal{V}}$: other terms are canceled by the cross product operation. γ is positive for a convex topography and negative otherwise. We thus obtain the classical expression of a centripetal force

$$\vec{F}_{\mathcal{H}} = c(\boldsymbol{\mathcal{V}}^t \partial^2_{\mathbf{XX}} b \boldsymbol{\mathcal{V}})\vec{n} = \gamma \|\vec{\mathcal{V}}\|^2 \vec{n}. \tag{30}$$

Note however that as for any acceleration force, the expression of the curvature force depends on the velocity parametrization. In the topography reference frame $(\vec{e}_1, \vec{e}_3, \vec{e}_3)$, the velocity components are given by $\vec{V}$. Provided we impose $V_3 = 0$, (15) describes the evolution of the 2D velocity field $\bar{\mathbf{V}}$ along the topography. The curvature force in this reference frame is exactly

$$\mathbf{F}_{\mathcal{H}}^{\bar{\mathbf{V}}} = -c\left(\bar{\mathbf{V}}^t(\partial^2_{\mathbf{XX}}b)\bar{\mathbf{V}}\right)\mathbf{s}. \tag{31}$$

$\mathbf{F}_{\mathcal{H}}^{\bar{\mathbf{V}}}$ has the direction of the main slope and can have a non-zero power ($\mathbf{F}_{\mathcal{H}}^{\bar{\mathbf{V}}} \cdot \bar{\mathbf{V}} \neq 0$). As a matter of fact, in the absence of gravity and friction, the kinetic energy must remain constant, however it is given by $\|\vec{\mathcal{V}}\|^2 = \|\bar{\mathbf{V}}\|^2 + \left(\frac{1}{c}\mathbf{s}^t\bar{\mathbf{V}}\right)$ and not by $\|\bar{\mathbf{V}}\|^2$ which is not constant, explaining why the curvature force has a non-zero power in the topography reference frame.

3.2 Comparison with previous studies

3.2.1 Friction force

If we use (30) in (23) to introduce the curvature along flow path γ in the friction force, we get

$$\vec{F}_\mu = -\frac{\mu\vec{\mathcal{V}}}{\|\vec{\mathcal{V}}\|}\left(gc + \gamma\|\vec{\mathcal{V}}\|^2\right)_+, \tag{32}$$

This is the classical expression of the friction force. In 1D (for $b = b(X)$), the derivation of γ is simple. Thus, most 1D thin-layer models [e.g. *Savage and Hutter*, 1991] include the curvature in the friction force. As shown in the previous section, the computation is less self-evident for real 2D topographies ($b = b(X, Y)$), in particular because the flow path must take into account velocity variations (see Supplementary Note 2). The curvature term in the friction force is thus either neglected [*O'Brien et al.*, 1993] or approximated. For instance, *Pitman et al.* [2003] use the curvature in the X and Y directions in the momentum equations for V_X and V_Y respectively. We could find only one reference (found in *Fischer et al.* [2012]) to the exact curvature expression mentioned above with a different numerical model than SHALTOP (that is based on the thin-layer equations derived previously). However, it is also possible to implicitly take into account this curvature by solving the equations for the pressure at the bottom of the flow, in addition to the flow thickness and velocity [*Rauter and Tukovic*, 2018, see next section].

If the curvature γ is positive, we see from (32) that neglecting the curvature decreases the bottom friction and accelerates the flow. The opposite effect is expected if γ is negative. On non-flat topographies, we can expect the flow to propagate on gradually decreasing slopes, at least in a first approximation. For instance, the longitudinal cross-sections of volcanoes are often modeled with an exponential fit [e.g. *Mangeney-Castelnau et al.*, 2003; *Kelfoun*, 2011; *Levy et al.*, 2015]. The topography is thus "globally" convex and the curvature is positive at most points. Without the curvature term in the friction, we can thus expect landslides to go further than in the model including curvature.

The effect of approximating the curvature depends of course on the chosen approximation. In Supplementary Note 2, we analyze these effects in some examples. In particular we can compute the curvature along topography in a straight direction given by the local velocity, that is, without taking into account changes in direction. If the flow is not moving in the main slope direction, then the curvature term will be over-estimated.

The numerical code Volcflow uses the following approximation (Karim Kelfoun, personnal communication),

$$\gamma = \gamma_x|\cos(\alpha)| + \gamma_y|\sin(\alpha)|, \tag{33}$$

where α is the angle between the horizontal component of the velocity and the X-axis. In our study, we shall test the approximation

$$\gamma = \gamma_x\cos^2(\alpha) + \gamma_y\sin^2(\alpha), \tag{34}$$

which is a more classical weighting as $\cos^2(\alpha) + \sin^2(\alpha) = 1$. In both cases, the model is no longer invariant by rotation. For instance, in the case of a flow confined to a channel, we show in Supplementary Note 2 that both approximations entail a deceleration of the flow in most realistic cases. When the channel is aligned with in the X or Y axes, the deviation from the exact equations is null, but significant differences can be expected otherwise. As the two previous approximations have similar effects, we will test only the second in the following. The effects of neglecting or approximating the curvature with (34) will be assessed in simulations in Sections 4 and 5.

3.2.2 Curvature force

The first detailed derivation of thin-layer equations for complex topographies was carried out by *Savage and Hutter* [1991] on 1D topographies. The curvature tensor $\mathcal{H}$ was reduced to a scalar κ, the curvature of the topography graph $Z = b(X)$. The curvature term is present in their final expression of the friction force, but no curvature force appears. That is however expected, given their parametrization. They use a curvilinear coordinate system (ξ, η), with η the distance from the topography (our coordinate x_3) and ξ the curvilinear coordinate along the topography graph. The associated orthonormal base is composed of the topography tangential vector $\vec{T}$ and of the topography normal vector $\vec{n}$. To be consistent with *Savage and Hutter* [1991], let us choose the new parametrization

$$\mathbf{u} = \frac{\bar{\mathbf{V}}}{c}. \tag{35}$$

This is equivalent to changing our topography reference frame to $(\vec{i}_1, \vec{i}_2, \vec{i}_3) = (c\vec{e}_1, c\vec{e}_2, \vec{e}_3)$, such that in 1D, $\vec{i}_1$ is the downslope unit vector and $(\vec{i}_1, \vec{i}_3)$ is an orthonormal base. With this parametrization, the physical velocity is $(c\mathbf{u}, \mathbf{s}^t\mathbf{u})$ and its norm is

$$\|\vec{\mathcal{V}}\|^2 = \|c\mathbf{u}\|^2 + (\mathbf{s}^t\mathbf{u})^2. \tag{36}$$

Substituting (35) in (15), we can show that the momentum equation for $\mathbf{u}$ is (17), where the curvature force becomes:

$$\mathbf{F}^{\mathbf{u}}_{\mathcal{H}} = -\frac{1}{c}\left(\mathbf{u}^t\mathcal{H}\mathbf{u}\right)\mathbf{s} + \frac{1}{c}\left(\mathbf{s}^t\mathcal{H}\mathbf{u}\right)\mathbf{u} \tag{37}$$

In comparison to (15), the new term $\frac{1}{c}\left(\mathbf{s}^t\mathcal{H}\mathbf{u}\right)\mathbf{u}$ comes from the computation of

$$(\bar{\mathbf{V}} \cdot \nabla_{\mathbf{X}})\bar{\mathbf{V}} = c(\nabla_{\mathbf{X}}(c\mathbf{u}))\mathbf{u}, \tag{38}$$

where $\partial_{\mathbf{X}} c$ appears. The curvature force is null when $\mathbf{s}$ and $\mathbf{u}$ are colinear (i.e. when the velocity is in the downslope direction). This is because in this case $\|\vec{\mathcal{V}}\| = \|\mathbf{u}\|$, so no correction needs to be applied to ensure energy is preserved. In particular in 1D, with this parametrization, no curvature forces appear in the equations.

Gray et al. [1999] derived thin-layer equations in a similar fashion. But instead of choosing a reference frame linked to the topography, they used a simpler reference surface with the constraint that the deviation from the topography is of the order $O(\epsilon)$, where ϵ is the ratio of a characteristic height of the flow over its characteristic length. In thin-layer models, ϵ is assumed to be very small (see Supplementary Note 1 for a discussion on the ordering of the equations, and for the mathematical meaning of $O()$). The same approach was used, for instance, by *George and Iverson* [2014]. This in turn makes it possible to assume that the velocity component normal to the reference surface (and not normal to the topography) has magnitude $O(\epsilon)$ and only the curvature of the reference surface needs to be accounted for. In *Gray et al.* [1999], this boils down to the curvature along the x-axis κ (see their equations (5.9) and (5.10)). With their ordering, it however disappears in the depth-averaged equations. The derivative of the curvature κ' also appears before the ordering of the equations in their work. It can also be found in the development of

Bouchut and Westdickenberg [2004] when curvilinear instead of cartesian coordinates are considered (without changing the accuracy of the resulting equations).

Another fine description of the topography was made by *Pudasaini and Hutter* [2003] for flows confined in channels. The thalweg is described by a 3D parametric curve $\vec{R}(s)$ to which an orthonormal reference frame is associated with the Serret-Frénet formulas. *Pudasaini and Hutter* [2003] write the Navier-Stokes equations in this reference frame. The topography curvature is then rendered by the curvature κ and torsion τ of the thalweg $\vec{R}(s)$. However, they thus describe only a limited set of topographies, making a proper comparison with our model difficult.

Fischer et al. [2012] derive a curvature force by solving the Euler-Lagrange equations for a free point mass m with coordinates $\vec{X}(t) = (X_1(t), X_2(t), X_3(t))$ subjected to gravity and evolving on the topography in a fixed cartesian reference frame. With our notation, the Lagrangian reads

$$L = \frac{1}{2} m \|\vec{X}(t)\|^2 - mgX_3(t), \tag{39}$$

with the constraint

$$f(\vec{X}) = X_3(t) - b(X_1, X_2) = 0. \tag{40}$$

Solving this system yields

$$\frac{d^2\vec{X}}{dt^2} = -gc^2 \begin{pmatrix} \nabla_{\mathbf{X}} b \\ \|\nabla_{\mathbf{X}} b\|^2 \end{pmatrix} + c \left(\boldsymbol{\mathcal{V}}^t \partial^2_{\mathbf{XX}} b \boldsymbol{\mathcal{V}} \right) \vec{n} = -gc^2 \begin{pmatrix} \nabla_{\mathbf{X}} b \\ \|\nabla_{\mathbf{X}} b\|^2 \end{pmatrix} + \vec{F}_{\mathcal{H}}. \tag{41}$$

This is the Lagrangian form of the momentum equation (20), without the friction force $\vec{F}_\mu$ and lateral pressure forces in $\vec{F}_g$. *Fischer et al.* [2012] use (41) to justify the curvature term appearing in the friction force, but the curvature force $\vec{F}_{\mathcal{H}}$ is actually independent of the friction.

Rauter and Tukovic [2018] and *Rauter et al.* [2018] use an approach similar to that of *Bouchut and Westdickenberg* [2004]. However, while we use the momentum equation for the topography-normal component of the velocity to get an explicit expression of the pressure, they keep this equation and consider the basal pressure as another unknown to be numerically estimated. This is equivalent to considering the basal pressure as a Lagrangian multiplier, respecting the constraint that the velocity is in the topography-tangent plane. With this method, *Rauter and Tukovic* [2018] do not need to explicitly describe the curvature. However, a rigorous derivation of their equations also requires complex differential calculations, in particular related to the definition of a gradient operator along the topography.

Now that we have detailed the origin of the curvature effects in thin-layer models, we will investigate their influence, in practice, in simulations. We will first consider simulations on synthetic topographies to identify situations where curvature effects significantly influences the results. We will then carry out simulations on real topographies.

4 Curvature effects in simulations with synthetic topographies

As shown in Section 3.1, the curvature force $\vec{F}_{\mathcal{H}}$ is needed to ensure that the flow velocity remains tangent to the topography. It is thus particularly important when the flow changes direction in twisted channels. As proposed by *Gray and Hutter* [1998], we create a synthetic topography with a channel composed of n_b successive bends, superimposed on a plane (Figure 3) with inclination $\theta = 10°$. The channel cross-section is a parabola (Figure 3b). At both extremities, there is a smooth transition between the end of the channel and the bottom plane (Figure 3a and 3c). The thalweg is a sinusoidal of amplitude A_b and period $L = 2.1$ m (black curve in Figure 3c). We define the ratio $\bar{\gamma} = A_b/(L/2)$, that can be seen as a non-dimensionalized bend curvature. This is detailed in Supplementary Note 3, along with the exact mathematical definition of this synthetic topography and some precisions on the simulation set-up.

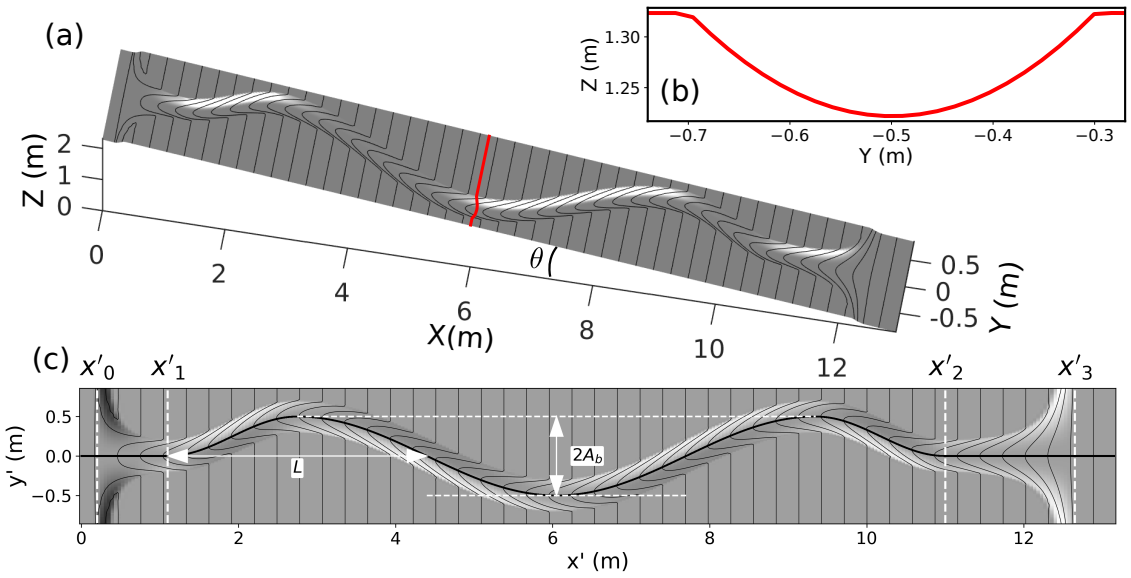

Figure 3. Synthetic topography with a twisted channel superimposed on a flat plane. (a) 3D view of the generated topography, in the fixed cartesian reference frame (b) Cross-section of the channel for $X = 6\ m$ (red curve in (a)). (c) Top view of the channel, with illustration of the parameters used to construct the topography are (see Supplementary Note 3). Here $L = 2.1$ m and $A_b = 0.5$ m. x' and y' are the curvilinear coordinates along the basal plane on which the channel is superimposed. The contour interval is 5 cm in both (a) and (b).

In the following, we will first investigate the effects of approximating curvature for a flow propagating in a straight channel (Section 4.1). We will then model flows in a channel with only one bend, with the Coulomb and the Voellmy rheologies and analyze how curvature affects the flow direction, velocity and kinetic energy (Section 4.2). For hazard assessment, however, it is convenient to synthesize the overall flow dynamics with a few simple characteristics. In Section 4.3, we will thus investigate curvature effects on the flow travel duration within the channel and on the maximal dynamic force, for various channel geometries and rheological parameters.

4.1 Curvature approximation and non-invariance by rotation

To demonstrate the importance of solving equations that are invariant by rotation, we first consider the propagation of a flow with the Coulomb rheology ($\mu = \tan(15°)$) and the Voellmy rheology ($\mu = \tan(15°)$ and $\xi = 2000$ m s^{-2}), in a channel without bends (that is, $A_b = 0$ m) and a slope inclination of $\theta = 10°$. As the flow propagates at the bottom of the channel, the curvature in the flow direction is, as a first approximation, zero. As a consequence, no curvature effects are expected. Changing the angle ϕ between the X-axis and the thalweg (see Figure 4a) should not change the flow dynamics. However, when we implement the approximation of the curvature (34) in the friction force, we lose the rotational invariance of the model and the flow is slowed down when $\phi > 0$ (Figure 4b to 4e). For instance with $\phi = 45°$, after 0.5 s, the total kinetic energy is decreased by 20% and 15%, with the Coulomb (Figure 4a) and Voellmy rheology (Figure 4c) respectively. This directly impacts the travel distance, with 20% (Figure 4b) and 5% (Figure 4d) reductions respectively.

In the following, we will no longer consider the approximation of curvature in the friction force, and compare only simulations when it is properly taken into account (which

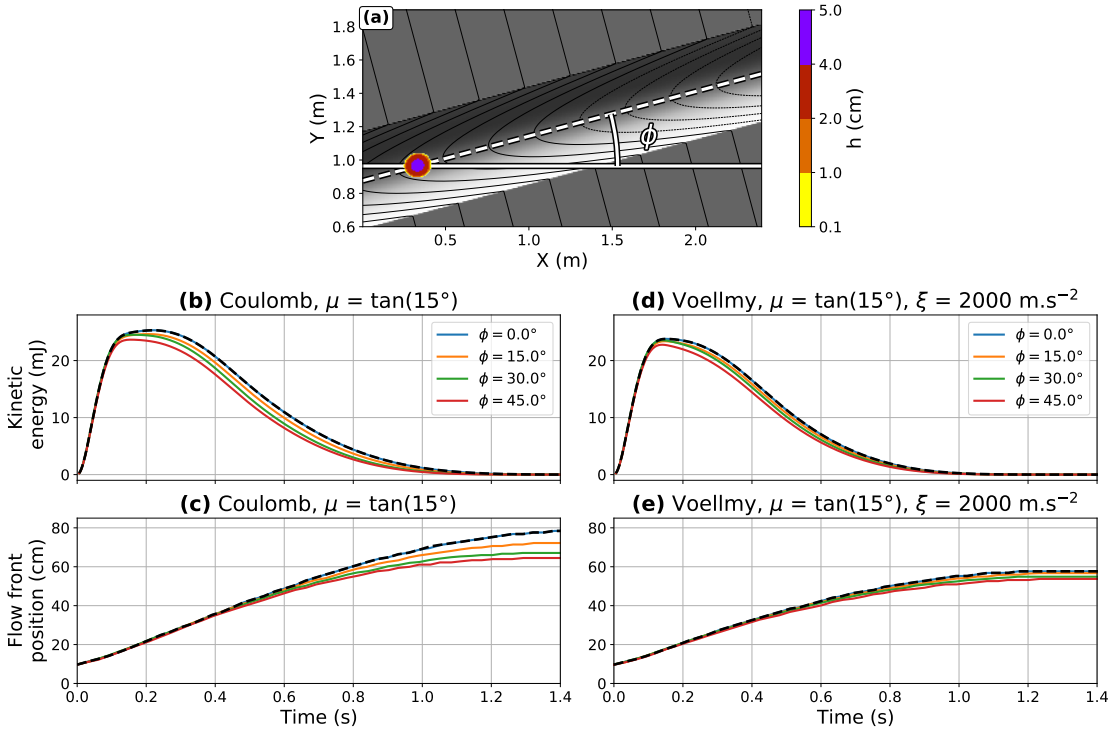

Figure 4. Modeling of a flow within a straight channel with inclination $\theta = 10°$. (a) Top view of the channel, with the initial mass (thickness is given by the color scale). ϕ is the angle between the channel direction (white dashed line) and the X-axis (white solid line). (b) and (c): Kinetic energy and flow front position, with the Coulomb rheology ($\mu = \tan(15°)$). Colored solid curves: results when the curvature term in the friction is approximated by weighting the curvature in the X and Y directions (see equation (34)), for different values of ϕ. Black dashed curves: result with the exact model, that does not depend on the channel orientation ϕ (up to small numerical errors, not shown here)as it should be. (d) and (e): Same as (b) and (c) but with the Voellmy rheology ($\mu = \tan(15°)$ and $\xi = 2000$ m s^{-2})

is not numerically costly) or omitted. Comparisons with approximated curvature are however provided in the Supplementary Figures and will be referred to briefly.

4.2 Thicknesses, velocity and kinetic energy

Let us now construct a channel with one bend of amplitude $A_b = 0.5$ m (and thus $\bar{\gamma} = 0.48$). We will first consider the case where $\mu = 0$ in the Coulomb rheology. We thus model a pure fluid and can highlight the influence of the curvature force, independently of the curvature term appearing in the friction force. This is however unrealistic when considering real geophysical flows, as there is no energy dissipation. We will thus also consider $\mu = \tan(6°)$, which is a sensible friction coefficient for debris flow modeling [e.g. *Moretti et al.*, 2015], and the Voellmy rheology that is commonly used to model such flows. To obtain insight on curvature effects for debris and rock avalanche modeling, we will finally model flows propagating on a steeper slope ($\theta = 25°$) with a higher friction coefficient $\mu = \tan(15°)$ [e.g. *Moretti et al.*, 2020].

4.2.1 Channel with slope $\theta = 10°$

For $\mu = 0$, the only acting forces are the curvature and gravity forces. The simulation results are displayed in Figure 5. As shown in Section 3.1, the curvature force horizontal component is in the steepest slope direction and thus tends to keep the flow at the bottom of the channel. This has a major impact on the flow direction at the exit of the channel (Figures 5a and 5b). It also results in a smoother increase of the flow velocity (Figure 5e, between 1 and 2 s), because without the curvature force, the flow bounces back and forth on the channels walls (Figures 5a and 5b). Thus, the effect of the curvature force cannot be neglected: its norm is indeed comparable to the norm of gravity and pressure forces when there are steep changes in the topography, as in the main bend and at the outlet of the channel (Supplementary Figures 1b and 1c). The maximum flow velocities are, however, of the same order: about 3 m s^{-1} at the outlet of the channel (Figures 5c and 5d).

In order to model debris flows more realistically, we now use a friction coefficient $\mu = \tan(6°)$. We can then analyze the influence of neglecting the curvature term in the friction force (Figures 6 , $\vec{F}_\mu$=0). Because of friction, the flow is decelerated compared to the case without friction (only 2 m s^{-1} at the channel outlet). The curvature terms (both in friction and curvature forces), which are proportional to the square of velocity, are then only half as high as gravity and pressure forces (see Supplementary Figures 2b and 2d). However, neglecting the curvature force does still slow down the flow, with a 5% kinetic energy decrease at the channel outage (Figure 6 i, $F_{\mathcal{H}}$=0). On the contrary, neglecting the curvature term in the friction force results in a slightly smaller friction force and thus increases the flow velocity (kinetic energy increased by 5% at the channel outage, Figure 6i, F_μ no curvature) and runout (e.g. Figures 6a and 6e). Approximating the curvature in the friction decelerates the flow, as expected (see Supplementary Figures 2 and 3).

In the literature, the empirical Voellmy rheology is also often used to model debris flows. We show in Supplementary Figures 4 and 5 that curvature effects have only limited influence with this rheology, which will be confirmed by further results.

4.2.2 Channel with slope $\theta = 25°$

The main slope of the channel and the parameters we have considered so far are reasonable estimates for modeling debris flows [e.g. *Moretti et al.*, 2015]. For debris and rock avalanches, it is more relevant to use steeper slopes and higher friction coefficients. In Figure 7, we investigate the curvature effects on a steeper slope ($\theta = 25°$) and for a higher friction coefficient $\mu = \tan(15°)$, which is still characteristic of mobile landslides [*Pirulli and Mangeney*, 2008]. The impact of neglecting curvature terms is qualitatively similar to the previous case with $\mu = \tan(6°)$, but errors are amplified (see Supplementary Figures 6 and 7 for the simulations with approximated curvature in friction). In particular, neglecting the curvature term in the friction leads to a significant acceleration of the flow: at the channel outlet, the total kinetic energy is increased by 70% (Figure 8a, $F_{\mathcal{H}}$ exact and F_μ no curvature). It can be directly correlated to the 30% error induced on the friction in the channel bends, when curvature is not taken into account (Figures 8b and 8d).

In the above simulations, we have shown that the direction of the flow at the channel outlet can change significantly when curvature effects are not accounted for. That is of course of prior importance in hazard mapping. In order to characterize the flow dynamics, two other indicators can refine the hazard assessment analysis.

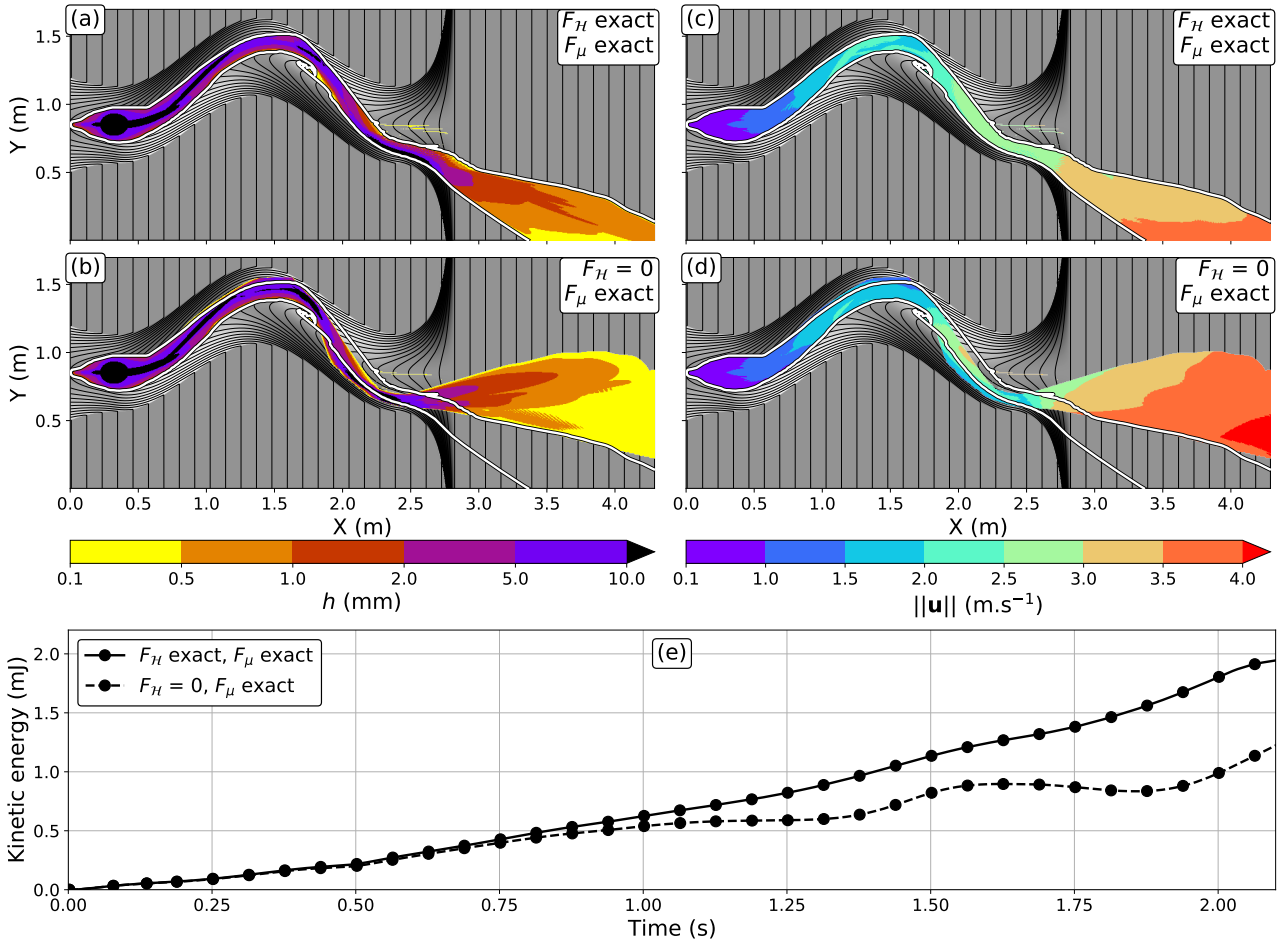

Figure 5. Flow simulation with the Coulomb rheology, $\mu = 0$ and a slope $\theta = 10°$. (a) and (c): with the curvature force ($F_{\mathcal{H}}$ exact). (b) and (d): without the curvature force ($F_{\mathcal{H}} = 0$). (a) and (b) give the maximum flow thickness during the simulation, (c) and (d) the maximum flow velocity. The white curve is the flow extent when the curvature force is taken into account. Simulation durations is 2.5 s. We give more details in Supplementary Note 4 on the derivation of maximum thickness and velocity maps.

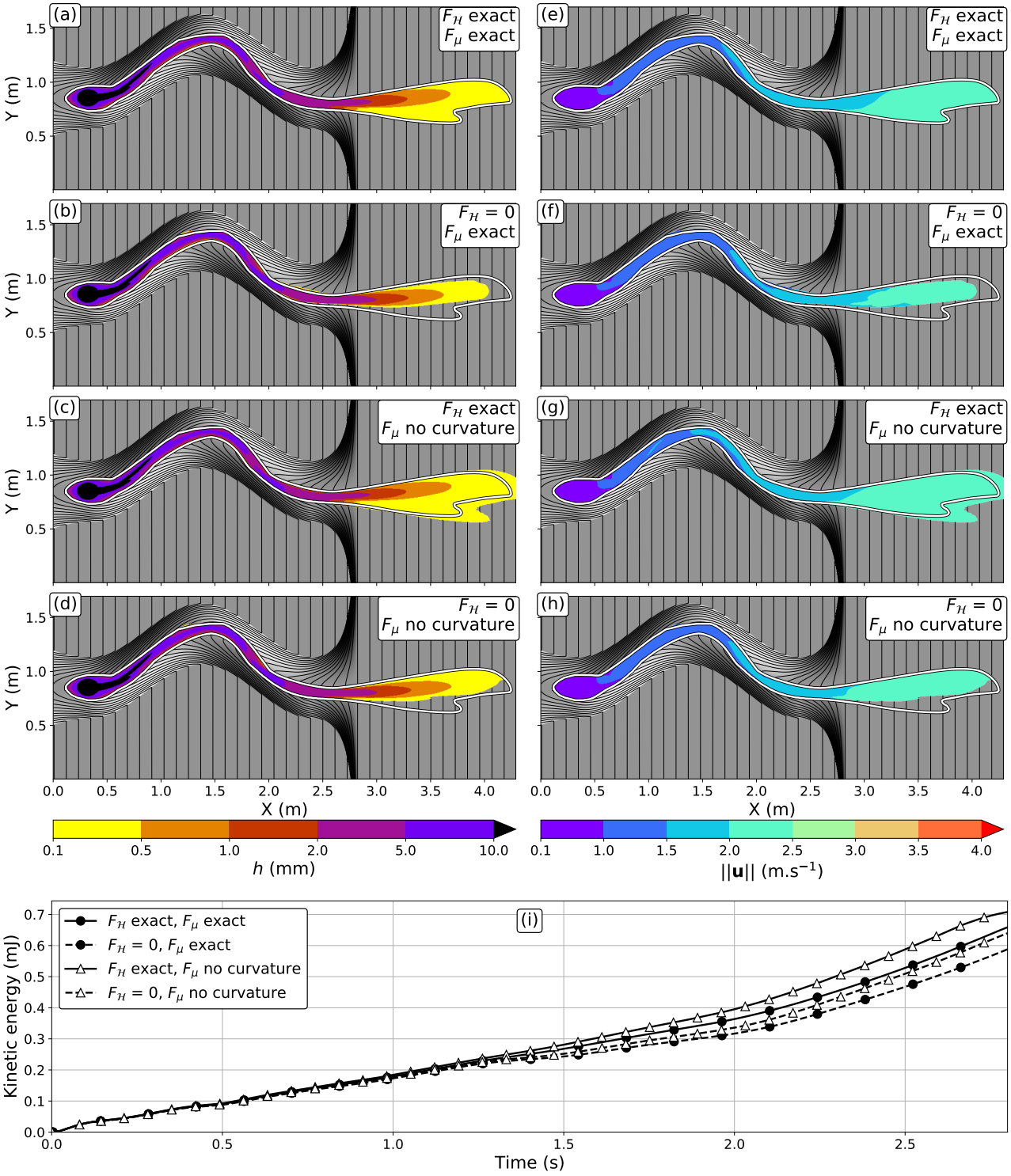

Figure 6. Flow simulation with the Coulomb rheology, $\mu = \tan(6°)$ and a slope $\theta = 10°$. The first column is the maximum flow thickness (a-d) and the second column is the flow maximum velocity (e-h), both after 2.8 s. Each subfigure displays the results of the simulation when the curvature force is taken into account ($F_{\mathcal{H}}$ exact) or neglected ($F_{\mathcal{H}} = 0$) and when the curvature in the friction is exact (F_μ exact) or neglected (F_μ no curvature). (a) and (e) are the simulation results in the reference case, with exact curvature terms: the corresponding flow extent (white line) is reported in all figures. The contour interval is 2 cm. (i) Kinetic energy in the different simulations.

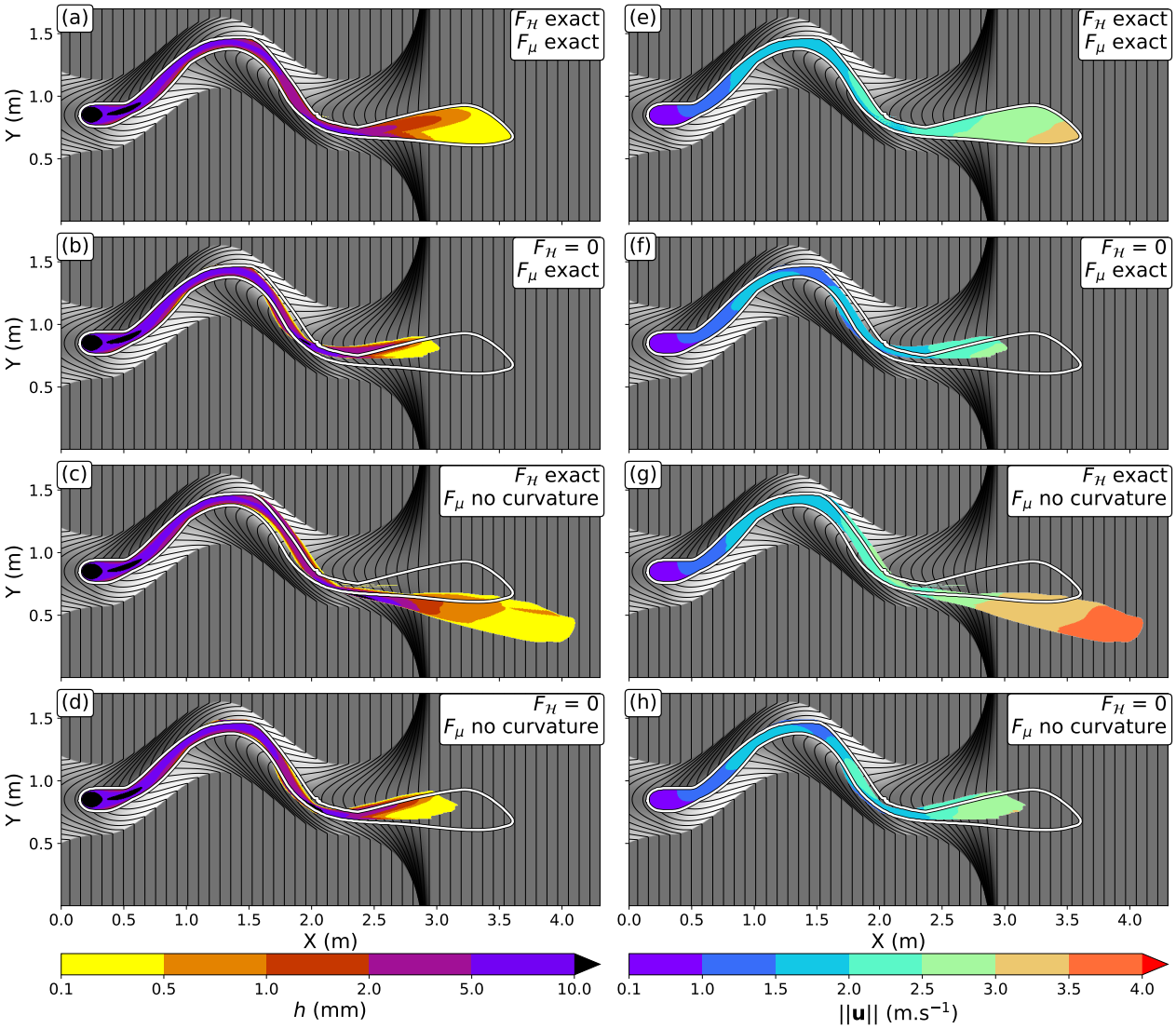

583 **Figure 7.** Same as 6, but with the Coulomb rheology, $\mu = \tan(15°)$ and a slope $\theta = 25°$. The contour inter-
584 val is 4 cm. Simulation duration is 2.3 s. The kinetic energies are given in Figure 8.

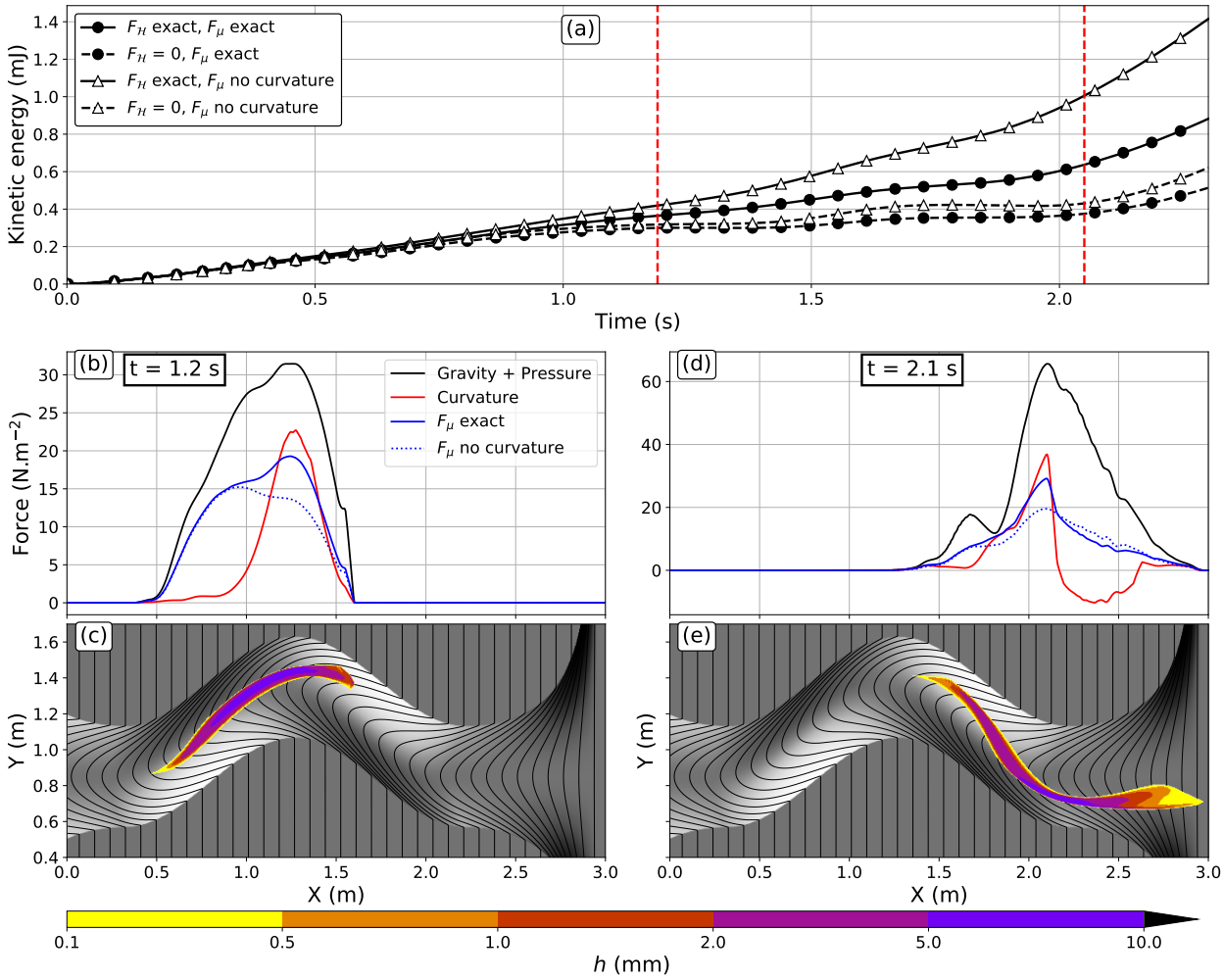

Figure 8. (a) Total kinetic energy of the flow with the Coulomb rheology, $\mu = \tan(15°)$ and a slope $\theta = 25°$. (b) For the simulation with exact curvature terms, maximum norm of gravity and pressure force ($\vec{F}_g^{\mathcal{V}}$, black curve), of the curvature force ($\vec{F}_{\mathcal{H}}^{\mathcal{V}}$, red curve, negative when $\vec{n} \cdot \vec{F}_{\mathcal{H}}^{\mathcal{V}} < 0$) and of the friction force ($\vec{F}_{\mathcal{H}}^{\mu}$, blue curves). The friction force is computed with the exact curvature term (F_μ exact) or when it is neglected (F_μ no curvature). The maximum is computed for a constant X coordinate, at t=1.2 s. (c) Flow thickness at t=1.2 s. (d) and (e): Same as (b) and (c), respectively, but for t=2.1 s. These two times are indicated by the red dashed vertical line in (a).

4.3 Travel time and maximum dynamic force

The flow travel duration within the channel is often a key indicator for hazard assessment. The second indicator is the maximum dynamic force F_d,

$$F_d = \max(\frac{1}{2}\rho h \|\vec{\mathcal{V}}\|^2) = \max(hP_d), \tag{42}$$

where P_d is the dynamic pressure. In the following we choose $\rho = 1500$ kg m^3 for the density: it acts only as a scaling factor. To obtain a more systematic analysis of the influence of curvature terms on these indicators, we keep only one bend, but try three different bend amplitudes: $A_b = 0$ m, $A_b = 0.25$ m and $A_b = 0.5$ m ($\bar{\gamma} = 0$, $\bar{\gamma} = 0.24$ and $\bar{\gamma} = 0.48$. Simulations are run in each configuration with the Coulomb and Voellmy rheologies, while varying the friction and turbulence coefficients.

Results are displayed in Figure 9 and summarized in Table 2. Unsurprisingly, for a straight channel, travel durations in the channel are very similar whatever the curvature description. There are however variations in the dynamic force (e.g. blues curves in Figure 9d), likely due to the initial spreading of the mass in all directions. When a bend is added ($A_b = 0.25$ m and $A_b = 0.5$ m), in the case of small friction coefficients and thus small friction forces, neglecting the curvature in the friction force has less effect than neglecting the curvature force (e.g. Figure 9a, $A_b = 0.5$ m for $\mu < \tan(6°)$). However the opposite occurs when the friction coefficient increases, as the friction force also increases. The error on maximum dynamic force is particularly high for fast flows, that is for small friction coefficients (e.g. for $A_b = 0.5$ m, up to 40% for $\mu = \tan(2°)$ and only 5% for $\mu = \tan(8°)$, Figure 9b). Note, however, that when we increase the length of the channel by adding successive bends, the effect of using incorrect curvature terms is amplified due to successive errors. We have for instance at most 5% discrepancies in travel durations with one bend and $\mu = \tan(6°)$, but up to 15% differences with 5 successive bends (see Table 2 and Supplementary Figure 8). With higher slope angles and friction coefficients corresponding to rock avalanches, the differences would be even more significant.

When we use the Voellmy rheology, as expected, differences in travel times are less striking: only 5% deviations for the flow travel time (Figure 9c), and 10% differences for the maximum dynamic force (Figure 9d).

We may wonder whether our observations on synthetic and simple topographies can be extrapolated to more realistic scenarios. In the next section, we thus carry out simulations on real topographies.

5 Curvature effects in simulations over real topographies

We chose two case studies for our simulations on real topographies: the simulation of debris flows in the Prêcheur river, in Martinique (French Caribbean) and the simulation of a debris avalanche on the Soufrière de Guadeloupe volcano, in Guadeloupe (French Caribbean)

5.1 Debris flow in the Prêcheur river

The Prêcheur river is located on the western flank of Montagne Pelée, an active volcano for which the last eruption dates back to 1932. Debris flows and hyper-concentrated flows occur regularly in this 6 km long river [*Clouard et al.*, 2013; *Nachbaur et al.*, 2019], with the risk of overflow into the Prêcheur village, at the mouth of the river [*Aubaud et al.*, 2013; *Quefféléan*, 2018]. In this context, numerical modeling can help constrain the prominent parameters controlling the flow dynamics and in turn be used for quantified risk assessment. However, a detailed analysis is beyond the scope of this paper. We only aim here to illustrate whether or not curvature effects have a significant impact on the flow dynamics. To that purpose, we release a hypothetical mass of 90,000 m^3 at the

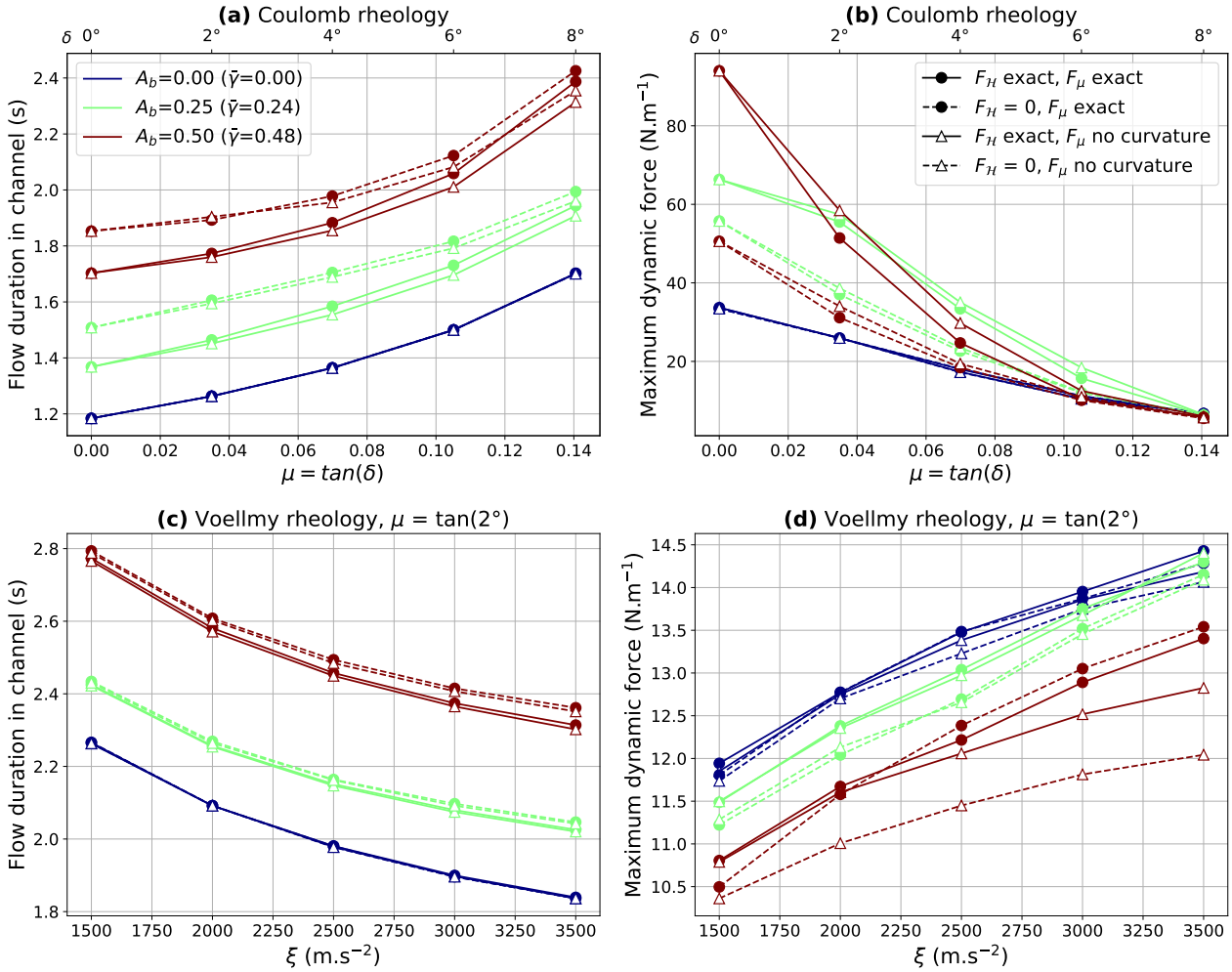

Figure 9. Simulation of a flow in a channel with slope $\theta = 10°$ and one bend with the Coulomb rheology (a and b) and the Voellmy rheology (c and d, with $\mu = \tan(2°)$). The bend amplitude A_b is either 0 m, 0.25 m or 0.5 m (respectively, blue, green and red curves).The corresponding non-dimensionalized curvature is $\bar{\gamma}$ The flow duration in the channel (a and c) and the maximum impact pressure (b and d) are plotted as functions of the friction coefficients for the Coulomb rheology (the top x-axis gives the corresponding friction angle) and as functions of the turbulence coefficient for the Voellmy rheology. Different situations are considered: when the curvature force is taken into account ($F_\mathcal{H}$ exact) or neglected ($F_\mathcal{H} = 0$) and when the curvature in the friction is exact (F_μ exact) or neglected (F_μ no curvature)

Table 2. Influence of curvature terms for synthetic topographies, with the Coulomb rheology, for different channel geometries with slope $\theta = 10°$ (lines, with A_b the channel bend amplitude) and friction coefficients (columns). The relative maximum deviation from the reference simulation with exact curvature is given for the flow duration in the channel (Δt, bold) and for the maximum dynamic force (F_d, italic). We specify which curvature term has the more prominent influence on the flow dynamics: the curvature force ($F_\mathcal{H}$) or the curvature in the friction (F_μ). n/a indicates indicates no simulation was done.

		$\mu = \tan(0°)$		$\mu = \tan(6°)$		$\mu = \tan(8°)$	
		Δt	F_d	Δt	F_d	Δt	F_d
$A_b = 0$ m		**0**%	*0*%	**0**%	*-5*%	**0**%	*0*%
$A_b = 0.25$ m	1 bend	**+10**%	*-15*%	**+5**%	*-25*%	**+2.5**%	*-5*%
		$F_\mathcal{H}$		$F_\mathcal{H}$		$F_\mathcal{H}$, F_μ	
$A_b = 0.5$ m	1 bend	**+10**%	*-45*%	**+5**%	*+20*%	**-2.5**%	*+5*%
		$F_\mathcal{H}$		$F_\mathcal{H}$, F_μ		F_μ	
	5 bends	not modeled		**+15**%[a] **-10**%[b]	*-60*%[a] *+135*%[b]	not modeled	
				F_μ			

[a] Differences for F_μ exact and $F_\mathcal{H} = 0$ neglected
[b] Differences for F_μ without curvature and $F_\mathcal{H}$ exact.

bottom of the cliff and model its propagation for 10 minutes, on a 5-meter Digital Elevation Model. We will first explore the possibility of overflows (Figures 10) in simulations with the Coulomb rheology. We will then conduct a more systematic analysis of curvature effects on the debris flow front position with the Coulomb and Voellmy rheologies and various rheological parameters, tracking the front position during the simulation with a thickness threshold of 1 cm (Figure 11). The results of approximating the curvature are displayed in Supplementary Figures 9 and 10.

5.1.1 Channel overflows with the Coulomb rheology

A critical point for hazard assessment is the possibility of overflows. In Figure 10, we show the maximum thickness of the flow in the Prêcheur river, simulated with the Coulomb rheology and $\mu = \tan(3°)$, which is representative of a highly mobile material. Keeping the curvature force but neglecting the curvature in the friction not only increases the runout, but also leads to multiple overflows (Figure 10c). Neglecting the curvature force partly compensates artificially this effect (Figure 10d). However, in this case, overflows dot not correspond to the ones modeled in the reference case (see Figure 10e and 10f, the white line is the extent of the flow in the simulation with exact curvature). Streaks outside the topography are artifacts explained in Supplementary Note 4.

5.1.2 Flow front position and travel distance

We now track the flow front position as the flow propagates in the river . With the Coulomb rheology, the travel distance is increased by several hundred meters when the curvature in the friction force is neglected (Figure 11a, solid and dashed curves with triangles). This difference may be reduced by choosing a thickness threshold higher than 1 cm. Nevertheless, it highlights the bias introduced by an improper curvature description. Curvature effects have a particularly strong influence in the upper part of the river which is narrow, twisted and with slopes above $\theta = 7°$ (see Figure 10): there are significant variations in the time needed by the flow to travel the first 1.5 km (Figure 11b). Depending on the friction coefficient, neglecting the curvature in the friction increases the flow veloc-

Table 3. Qualitative summary of the simulations results, with the different topographies (columns) and rheologies (lines). For the Coulomb rheology, we give the curvature description that gives the biggest error in comparison to simulations with the exact curvature. $F_{\mathcal{H}}$ refers to the curvature force and F_{μ} to the curvature in the friction force.

		Error max for channelized flow		**Error max for non-channelized flow**
		Synthetic topography	Prêcheur river	Soufrière de Guadeloupe
Coulomb	$\mu < \tan(5°)$	$F_{\mathcal{H}} = 0$	F_{μ} without curvature and $F_{\mathcal{H}}$ exact	*n/a*
	$\mu > \tan(5°)$	F_{μ} approximated	F_{μ} without curvature	F_{μ} without curvature
Voellmy		Limited influence of curvature effects		*n/a*

ity by 20 to 30% (Figure 11b, $F_{\mathcal{H}}$ exact, F_{μ} no curvature). This allows the flow to gain enough momentum to overrun flatter areas, whereas it remains stuck there in the reference case. To the contrary, neglecting the curvature force ($F_{\mathcal{H}} = 0$, F_{μ} exact) slows down the flow by 30 to 50%.

With the Voellmy rheology, the prominent factor impacting the flow dynamics is the curvature force (Figure 11d): without it, the flow needs up to 15% more time to travel the first 3 km. Further downstream, the delay between simulations is however constant (e.g. no more than 25 s with $\xi = 3500$ m s^{-2}, Figure 11c), which indicates once more that curvature effects affect the flow mainly in the upper part of the river.

5.2 Debris avalanche on the Soufrière de Guadeloupe volcano

Thin-layer numerical models are also commonly used to model the dynamics and emplacement of debris and rock avalanches, which are not confined to one channel as for debris flows. They usually involve bigger volumes (e.g. several million cubic meters) and spread on steeper slopes at least at their onset [e.g. *Guthrie et al.*, 2012]. In this section, we investigate the importance of curvature effects in simulations reproducing such events, studying the example of the Soufrière de Guadeloupe volcano, in Guadeloupe (French Caribbean). This volcanic edifice has a strong record of destabilization events, with at least 9 debris avalanches over the past 9,000 years [*Boudon et al.*, 2007; *Legendre*, 2012]. *Peruzzetto et al.* [2019] model the runout of a 90 $\times 10^6$ m^3 debris avalanche: this volume is consistent with the estimated volume (80 $\pm 40 \times 10^6$ m^3) of the 1530 CE debris avalanche . In order to reach the sea 9 km away from the volcano like the 1530 CE event, the friction coefficient $\mu = \tan(7°)$ had to be used (Figure 12a).

Using this friction coefficient and the same modeling set-up, we now model the debris avalanche emplacement by neglecting the different curvature terms (Figures 12b to 12f). The results of approximating the curvature are displayed in Supplementary Figure 11, and maximum kinetic energies in Supplementary Figure 12. When the curvature force is neglected, the most prominent difference is an excessive travel distance to the south (more than 1.5 km, Figure 12b , green rectangle). In some areas, spreading is less important, but only slightly (a difference of less than 200 m, Figure 12b, blue rectangle). Neglecting the curvature in the friction induces the most significant deviation from the reference simulation, with a generalized increase of the debris avalanche spreading (Figure 12c and 12d). In particular, the debris avalanche reaches the sea south of the Soufrière volcano, which is not predicted in the reference case (Figure 12a). Such differences are critical for tsunami hazard assessment.

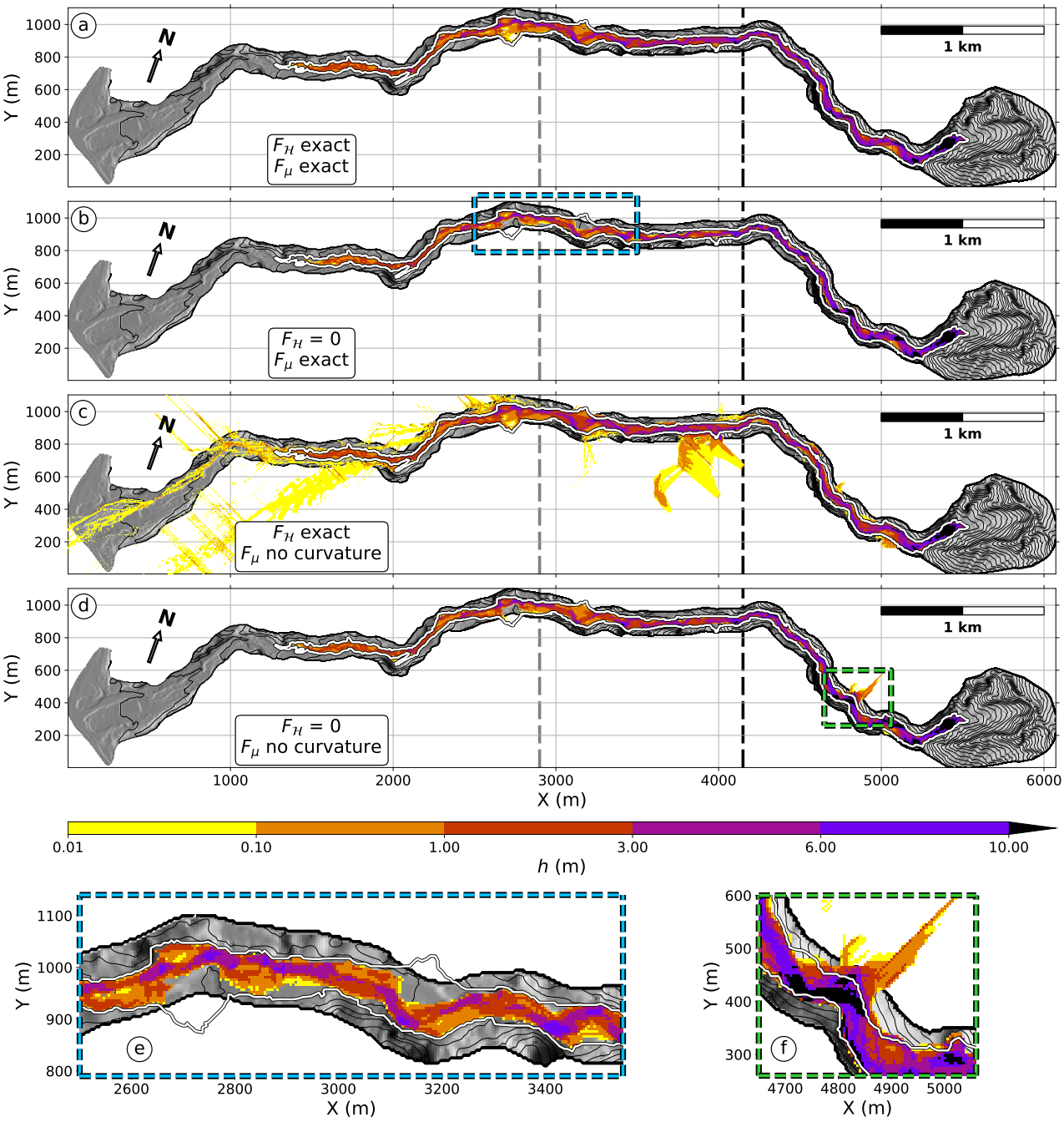

Figure 10. Maximum thickness of the flow simulated in the Prêcheur river with the Coulomb rheology and $\mu = \tan(3°)$. Each plot (a to d) displays the result of the simulation when the curvature force is taken into account ($F_\mathcal{H}$ exact) or neglected ($F_\mathcal{H} = 0$) and when the curvature in the friction is exact (F_μ exact) or neglected (F_μ no curvature). The simulation results in the reference case, with exact curvature terms, is given in (a). The corresponding flow extent (white curve) is reported in all figures. Green dashed rectangles (respectively blue dashed rectangles) indicate areas where the spreading is greater (respectively lesser) in other simulations, in comparison to the reference simulation (a). Zooms on these areas are given in (e) and (f). The contour step is 20 m.

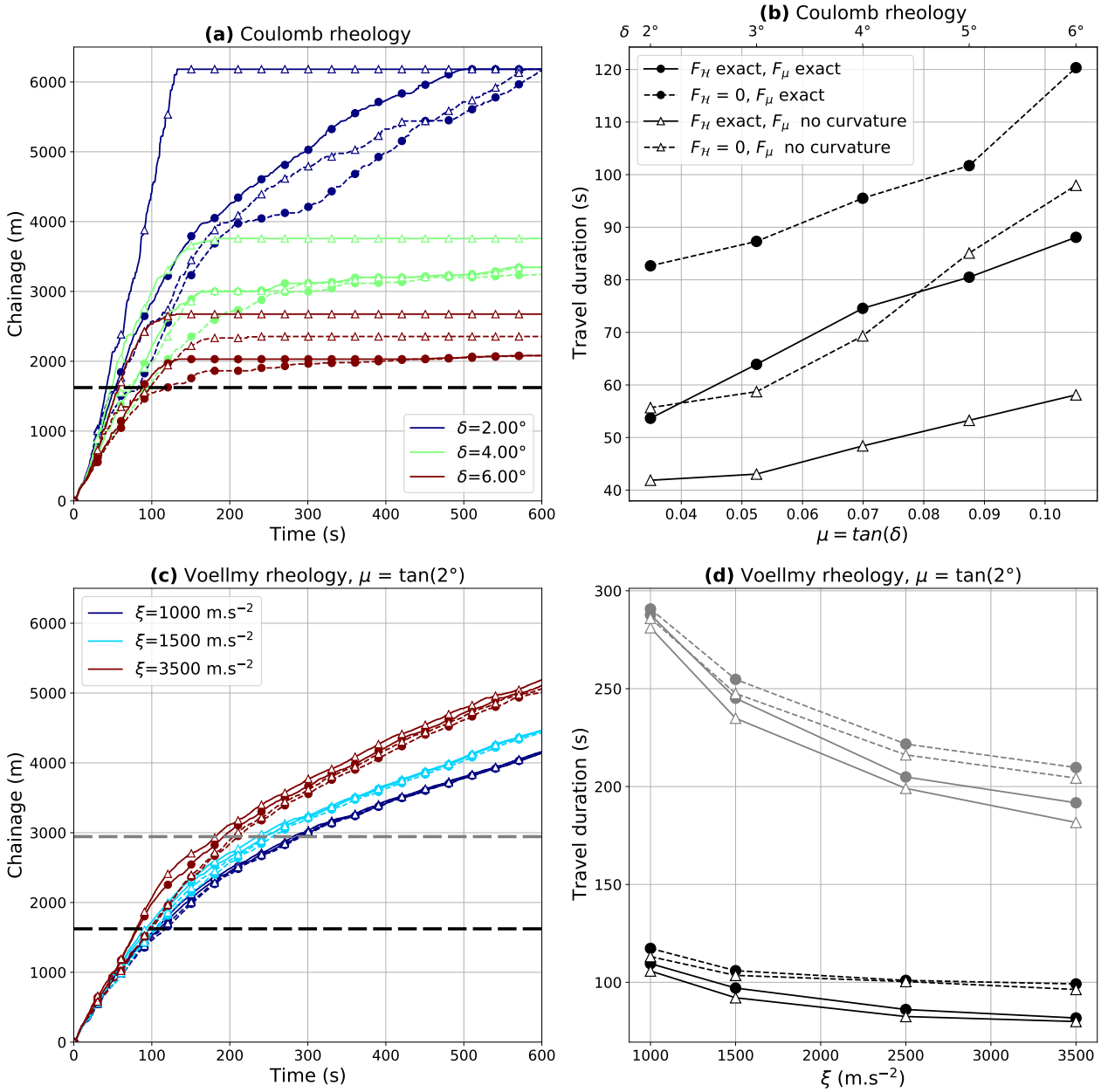

Figure 11. Simulations of debris flow in the Prêcheur river. Different situations are considered: when the curvature force is taken into account ($F_{\mathcal{H}}$ exact) or neglected ($F_{\mathcal{H}} = 0$) and when the curvature in the friction is exact (F_μ exact) or neglected (F_μ no curvature). (a) Flow front position with the Coulomb rheology. (b) Time needed for the flow to travel the first 1.6 km (black dashed line in (a)) with the Coulomb rheology, as a function of friction coefficient. (c) Flow front position with the Voellmy rheology and $\mu = \tan(2°)$. (d) Time needed for the flow to travel the first 1.6 km (black dashed line in (c)) and 2.9 km (gray dashed line in (c)) with the Voellmy rheology, as a function of turbulence coefficient.

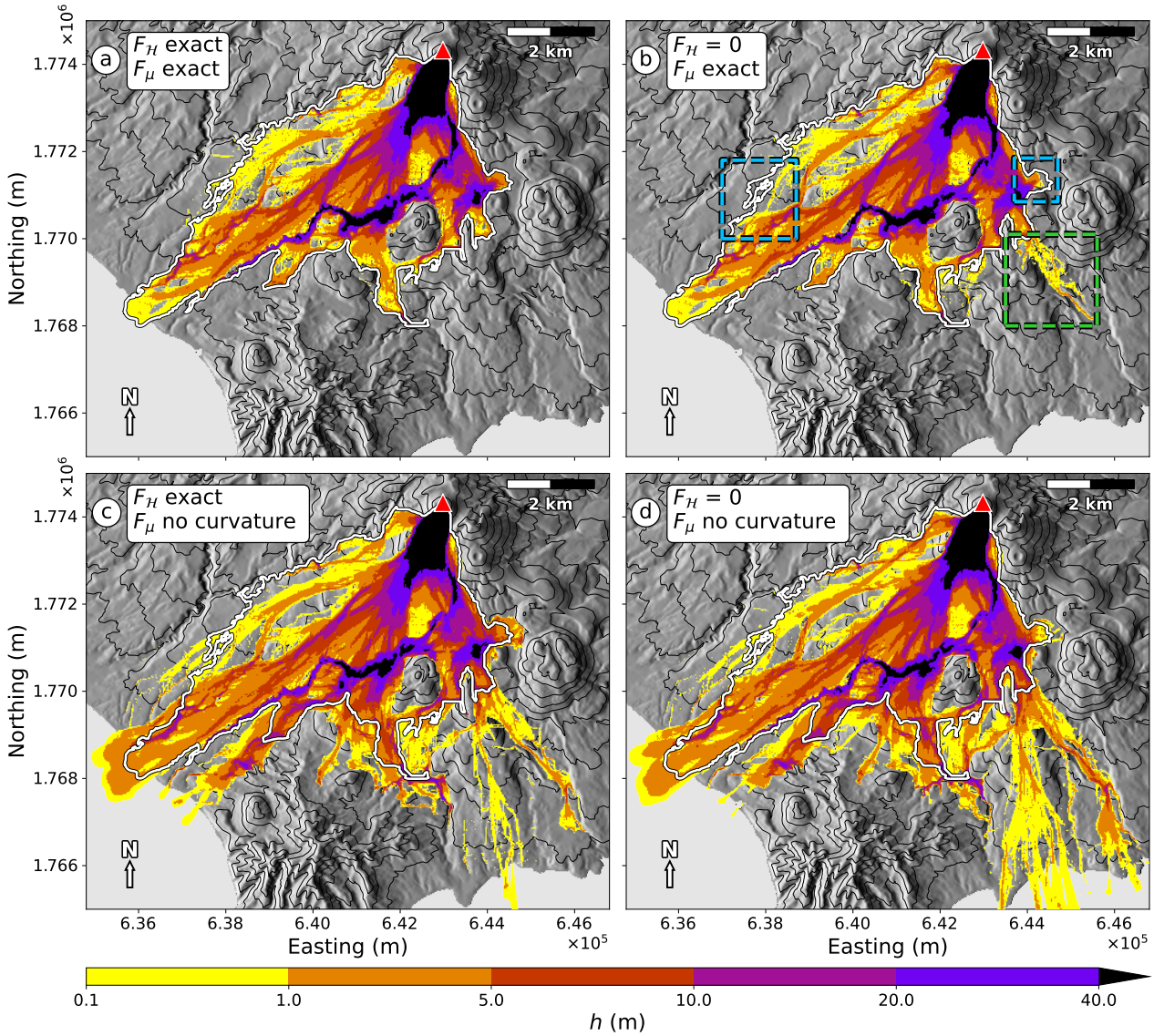

Figure 12. Maximum thickness of a hypothetical 90 $\times 10^6$ m^3 debris avalanche on the Soufrière de Guadeloupe volcano (French Caribbean). Each plot (a to f) displays the result of the simulation when the curvature force is taken into account ($F_{\mathcal{H}}$ exact) or neglected ($F_{\mathcal{H}} = 0$) and when the curvature in the friction is exact (F_{μ} exact) or neglected (F_{μ} no curvature). The simulation results in the reference case, with exact curvature terms, is given in (a) [*Peruzzetto et al.*, 2019]. The corresponding flow extent (white curve) is reported in all figures. Green dashed rectangles (respectively blue dashed rectangles) indicate areas where the spreading is greater (respectively lesser) in other simulations, in comparison to the reference simulation (a). The DEM is from IGN BDTopo, coordinates: WGS84, UTM20N. The contour interval is 100m.

6 Discussion

6.1 Importance of curvature effects for different rheologies

In our study, we derived curvature forces for the simplified case of a inviscid thin-layer flow. That is of course a simplification, as complex interactions between solid particles and between the solid and liquid phases can be expected (see *Delannay et al.* [2017] for a review). The formal derivation of SHALTOP equations requires, for instance, that the kinematic viscosity is small (see Supplementary Note 1), which can be questioned in practice for muddy debris flows. *Pastor et al.* [2004] and *Pastor et al.* [2009b] used the Bingham and Herschel-Bulkley theories to derive an implicit relation between the flow average velocity and the basal shear stress for simple shear flows on 1D topographies. Note that the resulting equations are similar to that of SHALTOP, provided we use an appropriate friction coefficient μ that depends on the thickness and on the flow velocity. A more comprehensive description of viscous flows is done by *Pudasaini and Mergili* [2019].

Historically, the first constitutive equations for 1D granular flows thin-layer models were linked to soil mechanics, with the introduction of an internal friction coefficient [*Savage and Hutter*, 1991; *Gray et al.*, 1999]. Some studies suggest that it is needed to model granular flows [*Hungr*, 1995; *Gray et al.*, 1999; *Pirulli et al.*, 2007]. This is, however, difficult to extend to complex 2D topographies, requiring simplifications [*Iverson and Denlinger*, 2001] or on the contrary the resolution of the complete stress state within the flow [*Denlinger and Iverson*, 2004]. Besides, *Gray et al.* [2003] show that a hydraulic approach without internal friction, as in our study, allows to reproduce accurately shock waves generated when granular materials flow around obstacles or over topography slope breaks.

Finally, the $\mu(I)$-rheology has been increasingly used over past years to model dry granular flows [e.g. *GDR MiDi*, 2004; *Jop et al.*, 2006]. Formal derivations have been done to derive its depth-integrated version but for simple topographies only [e.g. *Gray and Edwards*, 2014; *Baker et al.*, 2016].

More generally, following the classification of thin-layer models done by *Luca et al.* [2009b], our study shows that curvature effects are important when there is limited resistance to shearing in the flow. However, we did not consider situations where resistance to shearing increases and/or stresses acting on topography perpendicular planes become significant (e.g., when an internal friction coefficient is used). In such cases, it is nevertheless difficult to concile both a fine decription of the topography and of the rheology. For instance, the velocity profile in the normal variable is in general unknown and evolves with the flow [*Ionescu et al.*, 2015], such that assuming a velocity profile as in *Luca et al.* [2009b] may break down energy conservation. It becomes even more complex when we consider that the flow rheology can change during propagation [*Iverson*, 2003].

6.2 Importance of curvature effects in the Coulomb rheology

With the Coulomb rheology and without internal friction, our simulations show that curvature effects can be significant for fast flows (e.g. several m s^{-1}). For a given topography, the relative importance of the curvature force and of the curvature within friction strongly depends on the friction coefficient μ (see Table 3): when it increases, the friction force (and thus the curvature term within friction) prevails over the curvature term. In the extreme case $\mu = 0$, there is no friction and the curvature force has a strong influence on the flow dynamics. The transition between these two regimes occurs between $\mu = \tan(6°)$ and $\mu = \tan(8°)$ in our simulations on synthetic topographies for a slope $\theta = 10°$. It is not clear how much these transition values depend on the flow path and on the topography itself: neglecting the curvature force in the Prêcheur river simulations entails a significant acceleration of the flow even for $\mu = \tan(2°)$. The latter is however artificially compensated for when the curvature force is also neglected for friction coefficient below $\tan(4°)$.

This artificial compensation of two errors with competing effects (accelerating and decelerating the flow) is fortuitous and not at all a generality.

We did not focus on the effect of approximating the curvature in the friction force because it is actually straight-forward to implement the accurate curvature term. However, approximating the curvature does results in significant differences. On synthetic topographies with friction angles above $\mu = \tan(5°)$, the prominent error compared to the correct simulation is obtained when the curvature within friction is approximated (e.g., see Supplementary Figures 2, 7 and 8). However, on real topographies, the prominent error occurs when it is neglected (see Supplementary Figure 9 and 10 for the Prêcheur river, and Supplementary Figure 11 and 12 for Soufrière de Guadeloupe simulations). This difference may stem from the roughness of the terrain (which has locally high curvatures) that is not rendered in our smooth synthetic channel. Such local effects can then strongly affect the simulations results globally, impacting for instance the travel distance.

Reproducing the laboratory experiment from *Iverson et al.* [2004] yields similar conclusions as what we observed for synthetic and real topographies. In this experiment, a granular flow propagates in and irregular channel. We model it using friction coefficients calibrated by *Lucas* [2010] ($\mu = \tan(23°)$ in the channel and $\mu = \tan(26°)$ elsewhere). The channel is not significantly twisted: using the same notations as previously, we estimate a non-dimensionalized bend curvature $\bar{\gamma} = 0.15$. In comparison, we had $\bar{\gamma} = 0.48$ for our synthetic topographies. Thus, the flow path is rather straight in the channel and curvature effects are limited in the first 0.3 s of the simulations (see Supplementary Figure 14). However, the important slope break at the channel increases bottom friction when curvature is taken into account, and removing curvature accelerates the flow (see Supplementary Figure 15). Omitting the curvature force does change the final geometry of the mass but to a lesser extent. Indeed, the flow velocity remains globally in the direction of the topography slope. All these observations are in agreement with our results for synthetic channels. Future comparisons could be carried out by modelling experimental flows in twisted flumes, as in *Scheidl et al.* [2015].

Errors induced by inaccurate curvature description can be highly critical for model calibration. For instance, without curvature in friction, higher friction angles are needed to reproduce the previous experiments deposits (at least 3° higher, see Supplementary Figure 16). That could explain why, in the first JTC1 benchmarking exercise in 2007, SHALTOP used in many examples a lower friction coefficient than other thin-layer models [*Hungr et al.*, 2007].

6.3 Limited influence of curvature effects in the Voellmy rheology

In the Voellmy rheology, an empirical turbulence term proportional to the square of velocity is added to the basal friction. It slows down the flow, but it also minimizes the relative importance of curvature effects (that are also proportional to the square of velocity) when there are sudden changes in the flow direction. As a result, there are only slight changes in the flow runout when curvature effects are not accounted for. This is clearly seen in our simulations, both on synthetic and real topographies . In Supplementary Note 5, we give an example of a back-analysis of a debris flow simulated with the Voellmy rheology. Neglecting the curvature force influences only slightly the results.

However, *Salm* [1993] actually suggests that the turbulence coefficient ξ is proportional to the mean distance between irregularities on the topography. This distance can be seen as an estimate of the local topography radius of curvature. In the same perspective, in their guide book to avalanche modeling, *Salm et al.* [1990] advise choosing higher turbulence coefficients on rough topographies than on smooth topographies. More recently, *Gruber and Bartelt* [2007] calibrated a spatially varying turbulence coefficient by back-analysis of snow avalanches. As *Fischer et al.* [2012] point out, the resulting map of turbulence coefficients is strongly correlated to the topography curvature. This suggests that

the Voellmy rheology, or at least the Voellmy rheology with a turbulence coefficient correlated to the local topography curvature, might be a way of taking into account curvature effects empirically. However the resulting model cannot correctly reproduce the complexity of the interaction between the flow and the topography, in particular because the curvature force depends on the velocity direction and not only on its norm.

6.4 Importance of local curvature effects for overflows and runup estimations

For smooth topographies and channelized flows, we can expect some hazard indicators, such as the travel distance and the impacted area, to vary evenly when the simulation parameters span their variation ranges. This is no longer the case when the flow manages to overflow topographic barriers. Such non-linear behaviors and threshold effects are highly critical for hazard assessment and complicate hazard mapping [*Mergili et al.*, 2018]. They cannot be described by simple laws relating, for instance, the travel distance to the initial unstable volume [e.g. *Lucas et al.*, 2014; *Mitchell et al.*, 2019].

In our study, when we disregarded the curvature force in the simulation of the debris avalanche on Soufrière de Guadeloupe volcano, part of the material managed to overrun a plateau and enter a ravine. It could then spread much further (about 1.5 km, see Figure 12b). Such a behavior is however not systematic. For channelized flows, the curvature force tends to maintain the flow at the bottom of the channel, whereas it would otherwise bounce back and forth on its walls and potentially overflow the channel. However, in the long run, the curvature force allows the flow to move faster because it does not dissipate energy boucing back and forth on the channel banks. If a sudden twist is encountered further down, the flow may in turn have enough energy to overflow the channel banks, which would not be the case without the curvature force. We could reproduce such a situation in the Prêcheur river, with the Coulomb rheology and $\mu = \tan(2°)$ (see Supplementary Figure 13).

Local curvature effects are thus worth taking into account when considering debris flow runup against steep slopes [*Iverson et al.*, 2016] and on the outer bank of a channel bend [*Scheidl et al.*, 2015]. In the latter case, the runup (that is, the elevation difference between the inner and outer boundaries of the flow in the channel, as measured in the field) can be related to the flow velocity[*Prochaska et al.*, 2008; *Scheidl et al.*, 2015]. The runup and/or the deduced velocity can then be used to fit rheological parameters in thin-layer simulations. As they describe the dynamics of the flow in locations where we can expect strong curvature effects, the resulting best-fit parameters may depend significantly on whether or not these curvature effects are properly described in the model, even with the Voellmy rheology.

7 Conclusion

In this work, we show how an incorrect derivation of the thin-layer equations can lead to the omission of two curvature terms , originating from the expression of the pressure at the bottom of the flow. The first one, the curvature force, does not depend on the rheology and ensures that the flow velocity remains tangent to the topography. The second one appears in the bottom friction force (and thus only when frictional rheologies such as Coulomb or Voellmy are used). They are both proportional to the square of the flow velocity, but also depend on the velocity orientation and topography curvature tensor.

We have carried out simulations on synthetic and real topographies to highlight the influence of these curvature terms in thin-layer numerical simulations, with the code SHALTOP (see Table 3). The curvature terms are all the more important when the flow is fast (typically, several m s^{-1} to tens of m s^{-1}), that is for low friction coefficients and/or steep slopes.

For flows propagating in twisted channels modeled with the Coulomb rheology, the curvature force tends to maintain the flow at the bottom of the channel. Thus, neglecting it favors bouncing on the channel walls and reduces the propagation velocity. For instance, in the case of the upper section of Prêcheur river where slopes are higher than $\theta = 7°$, omitting the curvature force in simulations reduces the average velocity of channelized flow by 30%, for friction coefficients below $\mu = \tan(6°)$. Simulated overflows then differ, which is critical for hazard assessment.

Approximating the curvature in the friction force can break the rotational invariance of the model and slow down the flow. Neglecting the curvature in friction decreases the norm of the friction force and thus accelerates the flow, when the latter propagates from steep to more gentle slopes. It results in the most important errors when the flow velocity is in the main slope direction, and more generally on real topographies. For instance, in the case of the simulation of a debris avalanche on the Soufrière de Guadeloupe, travel distances are increased by several hundred meters. We observe similar effects on a synthetic channel with slope $\theta = 25°$ and $\mu = \tan(15°)$, with a 50% increase of the kinetic energy. Though such effects can sometimes be artificially compensated for by also neglecting the curvature force, it is not at all systematic and thus both terms need to be properly taken into account for correct model calibration.

Though we have focused on debris flows and debris avalanches modeling, our results could apply to other geophysical flows, such as moutain river stream flows [*Borthwick and Barber*, 1992; *Churuksaeva and Starchenko*, 2015] and concentrated and dilute pyroclastic currents [*Komorowski et al.*, 2013; *Kelfoun et al.*, 2017]. Curvature effects may also be important for modeling landslide-generated tsunamis, for which the thin-layer equations must be integrated in the direction normal to the topography for the landslide, and in the vertical direction for the fluid layer [*Ma et al.*, 2013; *Delgado-Sánchez et al.*, 2019].

Note that strong curvature effects may also be an inherent limitation of thin-layer models. Indeed, curvature forces are particularly strong when the topography curvature is high, as for instance in a narrow channel. However, in this case, the thin-layer assumption may no longer be valid. In order to discriminate between real curvature effects and numerical artifacts, comparisons with full 3D models where no approximations are done on the layer thickness could be conducted. Yet such comparisons exercises may prove difficult [e.g. *Pirulli et al.*, 2018].

Of course, our results must also be considered in regard of the rheology uncertainty, which is sometimes large. We believe future research should focus on both the developement of accurate physically-based rheologies with constrained realistic parameters, and on methodologies to properply describe topography effects. Such studies are complementary to, in turn, develop a model uniting both aspects.

Acknowledgments

We gratefully thank the French Ministère de la Transition Ecologique et Solidaire (MTES) and the BRGM for funding this work for 2017–2020 as well as the ERC contract ERC-CG-2013-PE10-617472 SLIDEQUAKES for its contribution. Numerical computations were performed on the S-CAPAD platform, IPGP, France. We also thank the staff of OVSM-IPGP, BRGM Guadeloupe and BRGM Martinique for their contribution to the work on the Prêcheur river, the staff of OVSG-IPGP for their contribution to work on Soufrière de Guadeloupe and the staff of the OVS (IPGP) for insightful discussions. General funding for the Observatoires Volcanologiques et Sismologiques (OVS, IPGP) is provided by IPGP as well as CNRS INSU (Service National d'Observation en Volcanologie, SNOV). We thank Karim Kelfoun (Observatoire Magma et Volcan, Clermont-Ferrand, France) for providing details on the Volcflow software. This study contributes to the Université de Paris ANR-18-IDEX-0001 IdEx initiative. This is IPGP contribution 4169.

The 25 m resolution Digital Elevation Model of Guadeloupe (BDAlti) was obtained courtesy of IGN (2004). DEAL Martinique funded the LIDAR acquisition of the Prêcheur topography in August 2018. The Joint Technical Committee on Natural Slopes and Landslides (JTC1) of the Federation of International Geo-engineering Societies (FedIGS) provided the data of the Yu-Tung debris flow (Supplementary Note 5). Synthetic topographies and initial mass are available at 10.5281/zenodo.3758125. The SHALTOP code has restricted access (contact authors for more information).

References

Armanini, A., L. Fraccarollo, and G. Rosatti (2009), Two-dimensional simulation of debris flows in erodible channels, *Computers & Geosciences*, *35*(5), 993–1006, doi:10.1016/j.cageo.2007.11.008.

Aubaud, C., J.-E. Athanase, V. Clouard, A.-V. Barras, and O. Sedan (2013), A review of historical lahars, floods, and landslides in the Precheur river catchment (Montagne Pelee volcano, Martinique island, Lesser Antilles), *Bulletin de la Societe Geologique de France*, *184*(1-2), 137–154, doi:10.2113/gssgfbull.184.1-2.137.

Baker, J. L., T. Barker, and J. M. N. T. Gray (2016), A two-dimensional depth-averaged mu(I)-rheology for dense granular avalanches, *Journal of Fluid Mechanics*, *787*, 367–395, doi:10.1017/jfm.2015.684.

Barré de Saint-Venant, A.-J.-C. (1871), Théorie du mouvement non permanent des eaux, avec application aux crues des rivières et à l'introduction des marées dans leur lit, *Comptes rendus hebdomadaires des séances de l'Académie des sciences*, *LXXIII*.

Beguería, S., T. W. J. Van Asch, J.-P. Malet, and S. Gröndahl (2009), A GIS-based numerical model for simulating the kinematics of mud and debris flows over complex terrain, *Natural Hazards and Earth System Science*, *9*(6), 1897–1909, doi:10.5194/nhess-9-1897-2009.

Berger, M. J., D. L. George, R. J. LeVeque, and K. T. Mandli (2011), The GeoClaw software for depth-averaged flows with adaptive refinement, *Advances in Water Resources*, *34*(9), 1195–1206, doi:10.1016/j.advwatres.2011.02.016.

Borthwick, A. G. L., and R. W. Barber (1992), River and reservoir flow modelling using the transformed shallow water equations, *International Journal for Numerical Methods in Fluids*, *14*(10), 1193–1217, doi:10.1002/fld.1650141005, _eprint: https://onlinelibrary.wiley.com/doi/pdf/10.1002/fld.1650141005.

Bouchut, F., and M. Westdickenberg (2004), Gravity driven shallow water models for arbitrary topography, *Communications in Mathematical Sciences*, *2*(3), 359–389.

Bouchut, F., A. Mangeney-Castelnau, B. Perthame, and J.-P. Vilotte (2003), A new model of Saint Venant and Savage–Hutter type for gravity driven shallow water flows, *Comptes Rendus Mathematique*, *336*(6), 531–536, doi:10.1016/S1631-073X(03)00117-1.

Bouchut, F., E. D. Fernández-Nieto, A. Mangeney, and P.-Y. Lagrée (2008), On new erosion models of Savage–Hutter type for avalanches, *Acta Mechanica*, *199*(1-4), 181–208, doi:10.1007/s00707-007-0534-9.

Bouchut, F., E. Fernández-Nieto, A. Mangeney, and G. Narbona-Reina (2015), A two-phase shallow debris flow model with energy balance, *ESAIM: Mathematical Modelling and Numerical Analysis*, *49*(1), 101–140, doi:10.1051/m2an/2014026.

Bouchut, F., E. D. Fernández-Nieto, A. Mangeney, and G. Narbona-Reina (2016), A two-phase two-layer model for fluidized granular flows with dilatancy effects, *Journal of Fluid Mechanics*, *801*, 166–221, doi:10.1017/jfm.2016.417.

Boudon, G., A. Le Friant, J.-C. Komorowski, C. Deplus, and M. P. Semet (2007), Volcano flank instability in the Lesser Antilles Arc: Diversity of scale, processes, and temporal recurrence, *Journal of Geophysical Research*, *112*(B8), doi:10.1029/2006JB004674.

Brunet, M., L. Moretti, A. Le Friant, A. Mangeney, E. D. Fernández Nieto, and F. Bouchut (2017), Numerical simulation of the 30–45 ka debris avalanche flow of Montagne Pelée volcano, Martinique: from volcano flank collapse to submarine em-

placement, *Natural Hazards*, *87*(2), 1189–1222, doi:10.1007/s11069-017-2815-5.

Christen, M., J. Kowalski, and P. Bartelt (2010), RAMMS: Numerical simulation of dense snow avalanches in three-dimensional terrain, *Cold Regions Science and Technology*, *63*(1-2), 1–14, doi:10.1016/j.coldregions.2010.04.005.

Christen, M., Y. Bühler, P. Bartelt, R. Leine, J. Glover, A. Schweizer, C. Graf, B. W. McArdell, W. Gerber, Y. Deubelbeiss, T. Feistl, and A. Volkwein (2012), Integral hazard managment using a unified software environment, in *12th Congress INTERPRAEVENT 2012*, p. 10, Grenoble, France.

Churuksaeva, V., and A. Starchenko (2015), Mathematical Modeling of a River Stream Based on a Shallow Water Approach, *Procedia Computer Science*, *66*, 200–209, doi:10.1016/j.procs.2015.11.024.

Clouard, V., J.-E. Athanase, and C. Aubaud (2013), Physical characteristics and triggering mechanisms of the 2009-2010 landslide crisis at Montagne Pelee volcano, Martinique: implication for erosional processes and debris-flow hazards, *Bulletin de la Societe Geologique de France*, *184*(1-2), 155–164, doi:10.2113/gssgfbull.184.1-2.155.

Delannay, R., A. Valance, A. Mangeney, O. Roche, and P. Richard (2017), Granular and particle-laden flows: from laboratory experiments to field observations, *Journal of Physics D: Applied Physics*, *50*(5), 053,001, doi:10.1088/1361-6463/50/5/053001.

Delgado-Sánchez, J. M., F. Bouchut, E. D. Fernández-Nieto, A. Mangeney, and G. Narbona-Reina (2019), A two-layer shallow flow model with two axes of integration, well-balanced discretization and application to submarine avalanches, *Journal of Computational Physics*, p. 109186, doi:10.1016/j.jcp.2019.109186.

Denlinger, R. P., and R. M. Iverson (2004), Granular avalanches across irregular three-dimensional terrain: 1. Theory and computation:, *Journal of Geophysical Research: Earth Surface*, *109*(F1), doi:10.1029/2003JF000085.

Favreau, P., A. Mangeney, A. Lucas, G. Crosta, and F. Bouchut (2010), Numerical modeling of landquakes: LANDSLIDES AND SEISMIC WAVES, *Geophysical Research Letters*, *37*(15), n/a–n/a, doi:10.1029/2010GL043512.

Fernández-Nieto, E., J. Garres-Díaz, A. Mangeney, and G. Narbona-Reina (2018), 2D granular flows with the mu(I) rheology and side walls friction: A well-balanced multilayer discretization, *Journal of Computational Physics*, *356*, 192–219, doi:10.1016/j.jcp.2017.11.038.

Fischer, J.-T., J. Kowalski, and S. P. Pudasaini (2012), Topographic curvature effects in applied avalanche modeling, *Cold Regions Science and Technology*, *74-75*, 21–30, doi:10.1016/j.coldregions.2012.01.005.

Froude, M. J., and D. N. Petley (2018), Global fatal landslide occurrence from 2004 to 2016, *Natural Hazards and Earth System Sciences*, *18*(8), 2161–2181, doi:10.5194/nhess-18-2161-2018.

Garres-Díaz, J., F. Bouchut, E. Fernández-Nieto, A. Mangeney, and G. Narbona-Reina (2020), Multilayer models for shallow two-phase debris flows with dilatancy effects, *Journal of Computational Physics*, *419*, 109,699, doi:10.1016/j.jcp.2020.109699.

GDR MiDi (2004), On dense granular flows, *The European Physical Journal E*, *14*(4), 341–365.

GEO (2011), Guidelines on the Assessment of Debris Mobility for Channelised Debris Flows, *Technical Guidance Note 29*, Geotechnical ENgineering office, Hong-Kong.

George, D. L., and R. M. Iverson (2014), A depth-averaged debris-flow model that includes the effects of evolving dilatancy. II. Numerical predictions and experimental tests, *Proceedings of the Royal Society A: Mathematical, Physical and Engineering Sciences*, *470*(2170), 20130,820, doi:10.1098/rspa.2013.0820.

Gray, J., and A. Edwards (2014), A depth-averaged -rheology for shallow granular free-surface flows, *Journal of Fluid Mechanics*, *755*, 503–534, doi:10.1017/jfm.2014.450.

Gray, J., M. Wieland, and K. Hutter (1999), Gravity-driven free surface flow of granular avalanches over complex basal topography, *Proceedings of the Royal Society of London A: Mathematical, Physical and Engineering Sciences*, *455*, 1841–1874.

Gray, J. M. N. T., and K. Hutter (1998), Physik granularer Lawinen, *Physik Journal*, *54*(1), 37–43, doi:10.1002/phbl.19980540110.

Gray, J. M. N. T., Y.-C. Tai, and S. Noelle (2003), Shock waves, dead zones and particle-free regions in rapid granular free-surface flows, *Journal of Fluid Mechanics*, *491*, 161–181, doi:10.1017/S0022112003005317.

Greve, R., and K. Hutter (1993), Motion of a Granular Avalanche in a Convex and Concave Curved Chute: Experiments and Theoretical Predictions, *Philosophical Transactions: Physical Sciences and Engineering*, *342*(1666), 573–600, publisher: The Royal Society.

Gruber, U., and P. Bartelt (2007), Snow avalanche hazard modelling of large areas using shallow water numerical methods and GIS, *Environmental Modelling & Software*, *22*(10), 1472–1481, doi:10.1016/j.envsoft.2007.01.001.

Guthrie, R. H., P. Friele, K. Allstadt, N. Roberts, S. G. Evans, K. B. Delaney, D. Roche, J. J. Clague, and M. Jakob (2012), The 6 August 2010 Mount Meager rock slide-debris flow, Coast Mountains, British Columbia: characteristics, dynamics, and implications for hazard and risk assessment, *Natural Hazards and Earth System Sciences*, *12*(5), 1277–1294, doi:https://doi.org/10.5194/nhess-12-1277-2012.

Hungr, O. (1995), A model for the runout analysis of rapid flow slides, debris flows, and avalanches, *Canadian Geotechnical Journal*, *32*(4), 610–623, doi:10.1139/t95-063.

Hungr, O., R. Fell, R. Couture, and E. Eberhardt (Eds.) (2005), *Landslide Risk Management*, CRC Press, google-Books-ID: VzjNBQAAQBAJ.

Hungr, O., N. Morgenstern, and H. Wong (2007), Review of benchmarking exercise on landslide debris runout and mobility modelling, in *Proceedingd of The 2007 International Forum on Landdslide Disaster Management*, Ho & Li.

Hungr, O., S. Leroueil, and L. Picarelli (2014), The Varnes classification of landslide types, an update, *Landslides*, *11*(2), 167–194, doi:10.1007/s10346-013-0436-y.

Hutter, K., and T. Koch (1991), Motion of a granular avalanche in an exponentially curved chute: experiments and theoretical predictions, *Philosophical Transactions of the Royal Society of London. Series A: Physical and Engineering Sciences*, *334*(1633), 93–138, doi:10.1098/rsta.1991.0004.

Ionescu, I. R., A. Mangeney, F. Bouchut, and O. Roche (2015), Viscoplastic modeling of granular column collapse with pressure-dependent rheology, *Journal of Non-Newtonian Fluid Mechanics*, *219*, 1–18, doi:10.1016/j.jnnfm.2015.02.006.

Iverson, R. M. (2003), The debris-flow rheology myth, in *3rd International Conference on Debris-Flow Hazards Mitigation: Mechanics, Prediction, and Assessment*, vol. 1, pp. 303–314.

Iverson, R. M. (2012), Elementary theory of bed-sediment entrainment by debris flows and avalanches, *Journal of Geophysical Research: Earth Surface*, *117*(F3), n/a–n/a, doi:10.1029/2011JF002189.

Iverson, R. M., and R. P. Denlinger (2001), Flow of variably fluidized granular masses across three-dimensional terrain: 1. Coulomb mixture theory, *Journal of Geophysical Research: Solid Earth*, *106*(B1), 537–552, doi:10.1029/2000JB900329.

Iverson, R. M., and D. L. George (2014), A depth-averaged debris-flow model that includes the effects of evolving dilatancy. I. Physical basis, *Proceedings of the Royal Society A: Mathematical, Physical and Engineering Sciences*, *470*(2170), 20130,819, doi:10.1098/rspa.2013.0819.

Iverson, R. M., M. Logan, and R. P. Denlinger (2004), Granular avalanches across irregular three-dimensional terrain: 2. Experimental tests, *Journal of Geophysical Research: Earth Surface*, *109*(F1), doi:10.1029/2003JF000084, _eprint: https://onlinelibrary.wiley.com/doi/pdf/10.1029/2003JF000084.

Iverson, R. M., D. L. George, and M. Logan (2016), Debris flow runup on vertical barriers and adverse slopes: Debris Flow Runup, *Journal of Geophysical Research: Earth Surface*, *121*(12), 2333–2357, doi:10.1002/2016JF003933.

Jop, P., Y. Forterre, and O. Pouliquen (2006), A constitutive law for dense granular flows, *Nature*, *441*(7094), 727–730, doi:10.1038/nature04801.

Kelfoun, K. (2011), Suitability of simple rheological laws for the numerical simulation of dense pyroclastic flows and long-runout volcanic avalanches, *Journal of Geophysical Research*, *116*(B8), doi:10.1029/2010JB007622.

Kelfoun, K., and T. H. Druitt (2005), Numerical modeling of the emplacement of Socompa rock avalanche, Chile, *Journal of Geophysical Research*, *110*(B12), doi:10.1029/2005JB003758.

Kelfoun, K., V. Gueugneau, J.-C. Komorowski, N. Aisyah, N. Cholik, and C. Merciecca (2017), Simulation of block-and-ash flows and ash-cloud surges of the 2010 eruption of Merapi volcano with a two-layer model: MODEL OF THE 2010 ERUPTION OF MERAPI, *Journal of Geophysical Research: Solid Earth*, *122*(6), 4277–4292, doi:10.1002/2017JB013981.

Knebelman, M. S. (1951), Spaces of Relative Parallelism, *Annals of Mathematics*, *53*(3), 387–399, doi:10.2307/1969562, publisher: Annals of Mathematics.

Koch, T., R. Greve, and K. Hutter (1994), Unconfined Flow of Granular Avalanches along a Partly Curved Surface. II. Experiments and Numerical Computations, *Proceedings: Mathematical and Physical Sciences*, *445*(1924), 415–435, tex.ids: koch_unconfined_1994-1 publisher: The Royal Society.

Komorowski, J.-C., S. Jenkins, P. J. Baxter, A. Picquout, F. Lavigne, S. Charbonnier, R. Gertisser, K. Preece, N. Cholik, A. Budi-Santoso, and Surono (2013), Paroxysmal dome explosion during the Merapi 2010 eruption: Processes and facies relationships of associated high-energy pyroclastic density currents, *Journal of Volcanology and Geothermal Research*, *261*, 260–294, doi:10.1016/j.jvolgeores.2013.01.007.

Kwan, J., and H. W. Sun (2007), Benchmarking exercise on landslide mobility modelling - runout analyses using 3dDMM, in *Proceedings of The 2007 International Forum on Landslide Disaster Management*, p. 22, Geotechnical Division, The Hong Kong Institution of Engineers, Hong Kong.

Law, R. P. H., J. S. H. Kwan, F. W. Y. Ko, and H. W. Sun (2017), Three-dimensional debris mobility modelling coupling smoothed particle hydrodynamics and ArcGIS, in *Proceedings of the 19 th International Conference on Soil Mechanics and Geotechnical Engineering*, p. 4, Seoul.

Legendre, Y. (2012), Reconstruction fine de l'histoire éruptive et scenarii éruptifs à la soufrière de Guadeloupe : vers un modèle intégré de fonctionnement du volcan, thesis, Paris 7.

LeVeque, R. J., D. L. George, and M. J. Berger (2011), Tsunami modelling with adaptively refined finite volume methods, *Acta Numerica*, *20*, 211–289, doi:10.1017/S0962492911000043.

Levy, C., A. Mangeney, F. Bonilla, C. Hibert, E. S. Calder, and P. J. Smith (2015), Friction weakening in granular flows deduced from seismic records at the Soufrière Hills Volcano, Montserrat, *Journal of Geophysical Research: Solid Earth*, *120*(11), 7536–7557, doi:10.1002/2015JB012151.

Luca, I., Y. C. Tai, and C. Y. Kuo (2009a), Non-cartesian, topography-based avalanche equations and approximations of gravity driven flows of ideal and viscous flows, *Mathematical Models and Methods in Applied Sciences*, *19*(01), 127–171, doi:10.1142/S0218202509003371.

Luca, I., K. Hutter, Y. C. Tai, and C. Y. Kuo (2009b), A hierarchy of avalanche models on arbitrary topography, *Acta Mechanica*, *205*(1-4), 121–149, doi:10.1007/s00707-009-0165-4.

Lucas, A. (2010), Dynamique des instabilités gravitaires par modélisation et télédétection: Applications aux exemples martiens, Theses, Institut de physique du globe de paris - IPGP.

Lucas, A., and A. Mangeney (2007), Mobility and topographic effects for large Valles Marineris landslides on Mars, *Geophysical Research Letters*, *34*(10), doi:

10.1029/2007GL029835.

Lucas, A., A. Mangeney, D. Mège, and F. Bouchut (2011), Influence of the scar geometry on landslide dynamics and deposits: Application to Martian landslides, *Journal of Geophysical Research*, *116*(E10), doi:10.1029/2011JE003803.

Lucas, A., A. Mangeney, and J. P. Ampuero (2014), Frictional velocity-weakening in landslides on Earth and on other planetary bodies, *Nature Communications*, *5*, doi:10.1038/ncomms4417.

Ma, G., J. T. Kirby, and F. Shi (2013), Numerical simulation of tsunami waves generated by deformable submarine landslides, *Ocean Modelling*, *69*, 146–165, doi:10.1016/j.ocemod.2013.07.001.

Mangeney, A., F. Bouchut, N. Thomas, J. P. Vilotte, and M. O. Bristeau (2007), Numerical modeling of self-channeling granular flows and of their levee-channel deposits, *Journal of Geophysical Research*, *112*(F2), doi:10.1029/2006JF000469.

Mangeney-Castelnau, A., J.-P. Vilotte, M.-O. Bristeau, B. Perthame, F. Bouchut, C. Simeoni, and S. Yerneni (2003), Numerical modeling of avalanches based on Saint Venant equations using a kinetic scheme, *Journal of Geophysical Research*, *108*(B11), 2527, doi:10.1029/2002JB002024.

McDougall, S. (2017), 2014 Canadian Geotechnical Colloquium: Landslide runout analysis — current practice and challenges, *Canadian Geotechnical Journal*, *54*(5), 605–620, doi:10.1139/cgj-2016-0104.

McDougall, S., and O. Hungr (2004), A model for the analysis of rapid landslide motion across three-dimensional terrain, *Canadian Geotechnical Journal*, *41*(6), 1084–1097, doi:10.1139/t04-052.

Mergili, M., J.-T. Fischer, J. Krenn, and S. P. Pudasaini (2017), r.avaflow v1, an advanced open source computational framework for the propagation and interaction of two-phase mass flows, *Geoscientific Model Development Discussions*, pp. 1–30, doi:10.5194/gmd-2016-218.

Mergili, M., B. Frank, J.-T. Fischer, C. Huggel, and S. P. Pudasaini (2018), Computational experiments on the 1962 and 1970 landslide events at Huascarán (Peru) with r.avaflow: Lessons learned for predictive mass flow simulations, *Geomorphology*, *322*, 15–28, doi:10.1016/j.geomorph.2018.08.032.

Mitchell, A., S. McDougall, N. Nolde, M.-A. Brideau, J. Whittall, and J. B. Aaron (2019), Rock avalanche runout prediction using stochastic analysis of a regional dataset, *Landslides*, doi:10.1007/s10346-019-01331-3.

Moase, E., A. Strouth, and A. Mitchell (2018), A comparison of different approaches for modelling a fine-grained debris flow at Seton Portage, British Columbia, Canada, *Hong Kong*, p. 4.

Moretti, L., K. Allstadt, A. Mangeney, Y. Capdeville, E. Stutzmann, and F. Bouchut (2015), Numerical modeling of the Mount Meager landslide constrained by its force history derived from seismic data, *Journal of Geophysical Research: Solid Earth*, *120*(4), 2579–2599, doi:10.1002/2014JB011426.

Moretti, L., A. Mangeney, F. Walter, Y. Capdeville, T. Bodin, E. Stutzmann, and A. Le Friant (2020), Constraining landslide characteristics with Bayesian inversion of field and seismic data, *Geophysical Journal International*, *221*(2), 1341–1348, doi:10.1093/gji/ggaa056.

Nachbaur, A., Y. Legendre, M. Lombard, and T. Dewez (2019), Caractérisation géologique et identification des mécanismes d'instabilité de la falaise Samperre, *Rapport final RP-68564-FR*, BRGM.

O'Brien, J. S., P. Y. Julien, and W. T. Fullerton (1993), Two-dimensional water flood and mudflow simulation, *Journal of hydraulic engineering*, *119*(2), 244–261.

Pastor, M., M. Quecedo, E. González, M. I. Herreros, J. A. F. Merodo, and P. Mira (2004), Simple Approximation to Bottom Friction for Bingham Fluid Depth Integrated Models, *Journal of Hydraulic Engineering*, *130*(2), 149–155, doi:10.1061/(ASCE)0733-9429(2004)130:2(149).

Pastor, M., B. Haddad, G. Sorbino, S. Cuomo, and V. Drempetic (2009a), A depth-integrated, coupled SPH model for flow-like landslides and related phenomena, *International Journal for Numerical and Analytical Methods in Geomechanics*, *33*(2), 143–172, doi:10.1002/nag.705.

Pastor, M., T. Blanc, and M. Pastor (2009b), A depth-integrated viscoplastic model for dilatant saturated cohesive-frictional fluidized mixtures: Application to fast catastrophic landslides, *Journal of Non-Newtonian Fluid Mechanics*, *158*(1-3), 142–153, doi:10.1016/j.jnnfm.2008.07.014.

Pastor, M., A. Yague, M. Stickle, D. Manzanal, and P. Mira (2018a), A two-phase SPH model for debris flow propagation, *International Journal for Numerical and Analytical Methods in Geomechanics*, *42*(3), 418–448, doi:10.1002/nag.2748.

Pastor, M., K. Soga, S. McDougall, and J. S. H. Kwan (2018b), Review of Benchmarking Exercise on Landslide Runout Analysis 2018, *Hong Kong*, p. 65.

Patra, A., A. Bauer, C. Nichita, E. Pitman, M. Sheridan, M. Bursik, B. Rupp, A. Webber, A. Stinton, L. Namikawa, and C. Renschler (2005), Parallel adaptive numerical simulation of dry avalanches over natural terrain, *Journal of Volcanology and Geothermal Research*, *139*(1-2), 1–21, doi:10.1016/j.jvolgeores.2004.06.014.

Peruzzetto, M., J.-C. Komorowski, A. L. Friant, M. Rosas-Carbajal, A. Mangeney, and Y. Legendre (2019), Modeling of partial dome collapse of La Soufrière of Guadeloupe volcano: implications for hazard assessment and monitoring, *Scientific Reports*, *9*(1), 1–15, doi:10.1038/s41598-019-49507-0.

Petley, D. (2012), Global patterns of loss of life from landslides, *Geology*, *40*(10), 927–930, doi:10.1130/G33217.1.

Pirulli, M., and A. Mangeney (2008), Results of Back-Analysis of the Propagation of Rock Avalanches as a Function of the Assumed Rheology, *Rock Mechanics and Rock Engineering*, *41*(1), 59–84, doi:10.1007/s00603-007-0143-x.

Pirulli, M., and M. Pastor (2012), Numerical study on the entrainment of bed material into rapid landslides, *Géotechnique*, *62*(11), 959–972, doi:10.1680/geot.10.P.074.

Pirulli, M., M.-O. Bristeau, A. Mangeney, and C. Scavia (2007), The effect of the earth pressure coefficients on the runout of granular material, *Environmental Modelling & Software*, *22*(10), 1437–1454, doi:10.1016/j.envsoft.2006.06.006.

Pirulli, M., A. Leonardi, and C. Scavia (2018), Comparison of depth-averaged and full-3D model for the benchmarking exercise on lanslide runout, *Hong Kong*, p. 14.

Pitman, E. B., and L. Le (2005), A two-fluid model for avalanche and debris flows, *Philosophical Transactions of the Royal Society A: Mathematical, Physical and Engineering Sciences*, *363*(1832), 1573–1601, doi:10.1098/rsta.2005.1596.

Pitman, E. B., C. C. Nichita, A. Patra, A. Bauer, M. Sheridan, and M. Bursik (2003), Computing granular avalanches and landslides, *Physics of Fluids*, *15*(12), 3638–3646, doi:10.1063/1.1614253.

Prochaska, A. B., P. M. Santi, J. D. Higgins, and S. H. Cannon (2008), A study of methods to estimate debris flow velocity, *Landslides*, *5*(4), 431–444, doi:10.1007/s10346-008-0137-0.

Pudasaini, S. P. (2012), A general two-phase debris flow model, *Journal of Geophysical Research: Earth Surface*, *117*(F3), doi:10.1029/2011JF002186.

Pudasaini, S. P., and K. Hutter (2003), Rapid shear flows of dry granular masses down curved and twisted channels, *Journal of Fluid Mechanics*, *495*, 193–208, doi:10.1017/S0022112003006141.

Pudasaini, S. P., and M. Mergili (2019), A Multi-Phase Mass Flow Model, *Journal of Geophysical Research: Earth Surface*, *124*(12), 2920–2942, doi:10.1029/2019JF005204, _eprint: https://agupubs.onlinelibrary.wiley.com/doi/pdf/10.1029/2019JF005204.

Pudasaini, S. P., W. Eckart, and K. Hutter (2003), Gravity-Driven Rapid Shear Flows of Dry Granular Masses in Helically Curved and Twisted Channels, *Mathematical Models and Methods in Applied Sciences*, *13*(07), 1019–1052, doi:10.1142/S0218202503002805.

Queffféléan, Y. (2018), Mission d'expertise ONF-RTM sur les lahars du Prêcheur, *Tech. rep.*, ONF-RTM.

Rauter, M., and Z. Tukovic (2018), A finite area scheme for shallow granular flows on three-dimensional surfaces, *Computers & Fluids*, *166*, 184–199, doi: 10.1016/j.compfluid.2018.02.017, arXiv: 1802.05229.

Rauter, M., A. Kofler, A. Huber, and W. Fellin (2018), faSavageHutterFOAM 1.0: depth-integrated simulation of dense snow avalanches on natural terrain with OpenFOAM, *Geoscientific Model Development*, *11*(7), 2923–2939, doi:10.5194/gmd-11-2923-2018.

Rosatti, G., and L. Begnudelli (2013), Two-dimensional simulation of debris flows over mobile bed: Enhancing the TRENT2D model by using a well-balanced Generalized Roe-type solver, *Computers & Fluids*, *71*, 179–195, doi: 10.1016/j.compfluid.2012.10.006.

Salm, B. (1993), Flow, flow transition and runout distances of flowing avalanches, *Annals of Glaciology*, *18*.

Salm, B., A. Burkard, and H. U. Gubler (1990), *Berechnung von Fliesslawinen: eine Anleitung fuer Praktiker mit Beispielen*, Eidgenössische Institut für Schnee- und Lawinenforschung, Weissfluhjoch/Davos, oCLC: 717831567.

Savage, S. B., and K. Hutter (1991), The dynamics of avalanches of granular materials from initiation to runout. Part I: Analysis, *Acta Mechanica*, *86*(1), 201–223.

Scheidl, C., B. W. McArdell, and D. Rickenmann (2015), Debris-flow velocities and superelevation in a curved laboratory channel, *Canadian Geotechnical Journal*, *52*(3), 305–317, doi:10.1139/cgj-2014-0081.

Voellmy, A. (1955), Uber die Zerstorungskraft von Lawinen., *Schweizerische Bauzeitung, Jahrg.*, *73*, 159–162,212–217,246–249,280–285.

Wieland, M., J. M. N. T. Gray, and K. Hutter (1999), Channelized free-surface flow of cohesionless granular avalanches in a chute with shallow lateral curvature, *Journal of Fluid Mechanics*, *392*, 73–100, doi:10.1017/S0022112099005467.

Yavari-Ramshe, S., and B. Ataie-Ashtiani (2016), Numerical modeling of subaerial and submarine landslide-generated tsunami waves—recent advances and future challenges, *Landslides*, *13*(6), 1325–1368, doi:10.1007/s10346-016-0734-2.